

Liouvillean Spectral Transition in Noisy Quantum Many-Body Scars

Jin-Lou Ma,^{1,*} Zexian Guo,^{1,*} Yu Gao,¹ Zlatko Papić,^{2,†} and Lei Ying^{1,‡}

¹*School of Physics and Zhejiang Key Laboratory of Micro-nano Quantum Chips and Quantum Control, Zhejiang University, Hangzhou 310027, China*

²*School of Physics and Astronomy, University of Leeds, Leeds LS2 9JT, United Kingdom*
(Dated: April 17, 2025)

Understanding the behavior of quantum many-body systems under decoherence is essential for developing robust quantum technologies. Here, we examine the fate of weak ergodicity breaking in systems hosting quantum many-body scars when subject to local pure dephasing—an experimentally relevant form of environmental noise. Focusing on a large class of models with an approximate $\text{su}(2)$ -structured scar subspace, we show that scarred eigenmodes of the Liouvillean exhibit a transition reminiscent of spontaneous \mathbb{PT} -symmetry breaking as the dephasing strength increases. Unlike previously studied non-Hermitian mechanisms, this transition arises from a distinct quantum jump effect. Remarkably, in platforms such as the XY spin ladder and PXP model of Rydberg atom arrays, the critical dephasing rate shows only weak dependence on system size, revealing an unexpected robustness of scarred dynamics in noisy quantum simulators.

Introduction—Recent advances in quantum simulations [1–5] have opened a window to studying thermalization in isolated quantum many-body systems [6–10]. Many such systems are now understood to host atypical non-thermalizing eigenstates known as quantum many-body scars (QMBSs) [11–13]. QMBSs are ubiquitous in many physical platforms, including Rydberg atom arrays [14–28], the Heisenberg-type spin models [29–32], ultracold atoms in tilted optical lattices [33–38], superconducting circuits [39, 40], and many other [41–59]. An important class of QMBSs are those associated with a so-called ‘restricted $\text{su}(2)$ spectrum generating algebra’ (RSGA) [60–63], whereby scarred eigenstates distribute with nearly equal energy spacings and often have large overlap with product states. The unique properties of this class of QMBSs are of interest in quantum information processing [64–66], e.g., they have been used to generate Greenberger-Horne-Zeilinger (GHZ) states [67] and disorder-tunable entanglement [68].

The existing platforms for quantum simulation, however, are prone to decoherence caused by the surrounding environment. The decoherence – particularly pure dephasing – can significantly impact individual qubits [69], limiting their useful lifetime to around $10 \mu\text{s}$ in current state-of-the-art superconducting platforms [70]. While dissipation was studied in kinetically-constrained models [71, 72] and time crystals [73–76], its impact on the robustness of QMBS states remains poorly understood [77–79]. For example, while Ref. [77] recently demonstrated a construction for embedding QMBS into decoherence-free subspaces, a comprehensive understanding of realistic decoherence effects, such as pure dephasing, remains elusive. Previous studies of QMBSs to perturbations in closed systems [80, 81] suggest that QMBSs might quickly thermalize in the presence of noise.

In this paper, we consider a large class of models possessing a QMBS subspace with an $\text{su}(2)$ RSGA and coupled to the environment via local pure dephasing γ on

each site, see Fig. 1(a). In the presence of dissipation, it will be important to distinguish the cases where the RSGA is exact versus only approximately obeyed within the QMBS subspace. The former is characteristic of analytical models of QMBSs [60–62], while the latter describes various experimental realizations [14, 37, 39, 68]. In contrast to exact QMBSs, we find that approximate QMBSs undergo a process resembling spontaneous Liouvillean \mathbb{PT} -symmetry (LPTS) breaking at a non-zero dephasing rate γ_\star^S . Notably, we will argue that γ_\star^S for approximate QMBSs depends only polynomially on system size, in stark contrast with chaotic systems where γ_\star is inversely proportional to the square of the Liouvillean eigenvalue density [82]. This difference in scaling suggests that approximate QMBSs can maintain LPTS and dynamical scar signatures at finite dephasing rates in much larger systems than naively expected. We identify the origin of this phenomenon in the quantum jumper effect beyond previously considered non-Hermitian mechanisms [83, 84]. We illustrate our conclusions using the experimentally relevant model of superconducting qubit ladders [39], while in Appendix we provide further evidence for the PXP model of Rydberg atom arrays [14].

Quantum Liouvillean spectra—The Hamiltonian of a QMBS system can be written as $\hat{H} = \hat{S}_0 \oplus \hat{T} + \hat{V}$, where \hat{S}_0 and \hat{T} denote the Hamiltonian of scar and thermal subsystems, respectively, while \hat{V} represents the coupling between them [11], as illustrated in Fig. 1(a). Exact QMBS case corresponds to $\hat{V} = \hat{0}$ since the two sectors are completely decoupled, while approximate QMBSs correspond to $\hat{V} \neq \hat{0}$. The eigenvalues and eigenstates of an isolated system (with the total Hamiltonian \hat{H}) are denoted by E_n and $|E_n\rangle$, $n = 1, 2, \dots, D$, with D being the Hilbert space dimension. Among these, the QMBS eigenstates are denoted by $|E_{ns}\rangle$, while $|E_{nT}\rangle$ denotes the remaining thermal eigenstates. Notice that these eigenstates cannot be directly obtained from the subsystem Hamiltonians in the approximate QMBS case.

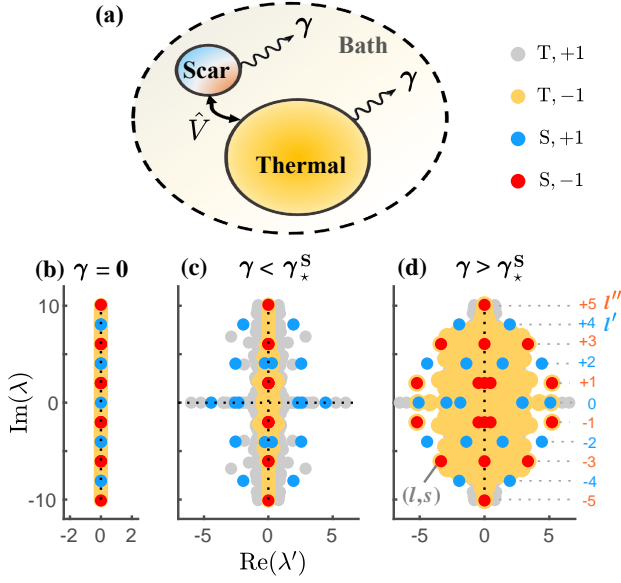


Figure 1. (a) Schematic of a general open quantum system with approximate QMBSs. The scar and thermal subsystems lose their quantum coherence to the bath with the dephasing rate γ , while interacting via the coupling \hat{V} . (b)-(d) The Liouvillean spectral transition in the SCL model, Eq. (2), for three different dephasing strengths $\gamma = 0, 0.0005$, and 0.02 . Red and blue dots represent scar (S) eigenvalues, while yellow and gray ones represent thermal (T) eigenvalues, labeled according to their inversion symmetry quantum number, $p = \pm 1$. In panel (d), (l, s) represents the s th eigenvalue in the l th layer [see text below Eq. (4)]. The scar eigenvalues in the l'' th layer undergo LPTS breaking as γ increases, while those in the l' th layer do not [compare red dots in panel (c) with (d)]. The data in (b)-(d) is obtained by exact diagonalization for the choice of couplings $J_h = 0.66$, $J_{x,j} = 0.1$, system size $L = 10$ with open boundary conditions.

We now consider each site to have individual decoherence to a bath. Under the Markov approximation, such a system is generally described by a Liouville superoperator [85]. Here, we focus on pure dephasing, with the corresponding superoperator

$$\begin{aligned} \mathcal{L} &= -i \left(\hat{H} \otimes \hat{I} - \hat{I} \otimes \hat{H}^* \right) + \gamma \mathcal{D}, \\ \mathcal{D} &= \mathcal{D}' - \sum_j \hat{I}_j \otimes \hat{I}_j, \quad \mathcal{D}' = \sum_j \hat{\sigma}_j^z \otimes \hat{\sigma}_j^z \end{aligned} \quad (1)$$

where γ is the pure dephasing rate and $\hat{\sigma}_j^z$ is a local jump operator on j th lattice site. The operator $|E_n\rangle\langle E_m|$ in \mathcal{L} has a vector representation given by $|E_n\rangle\langle E_m|$ [85]. The k th eigenvalue and eigenmode of the Liouville superoperator in Eq. (1) are denoted by λ_k and $|\lambda_k\rangle\rangle$, respectively, with $k = 1, 2, \dots, D^2$.

To understand the spectral properties of \mathcal{L} , we follow Ref. [82] and perform a transformation, $\mathcal{L}' = \mathcal{L} + \gamma(\text{Tr}(\mathcal{D})/\text{Tr}(\mathcal{I}))\mathcal{I}$, with $\mathcal{I} = \hat{I} \otimes \hat{I}$, which makes the Liouvillean spectrum traceless, i.e., sets the average of $\text{Re}(\lambda'_k)$ to zero. For an isolated system ($\gamma = 0$), the

spectrum is purely imaginary, $\text{Im}(\lambda_k) = E_n - E_m$, and $|\lambda_k\rangle\rangle = |E_n\rangle \otimes |E_m\rangle$. As we turn on dephasing, the eigenvalues on the imaginary axis move towards each other and collide, jumping into the complex plane [82]. This general picture of Liouvillean spectral evolution is illustrated in Fig. 1(b)-(d) for the example of the SCL model that we study in detail next.

SCL model—The SCL model describes spin-1/2 XY chains in a Cruetz ladder configuration [39, 86]. The Hamiltonian, $\hat{H}_{\text{SCL}} = \hat{H}_{h,1} + \hat{H}_{h,2} + \hat{H}_v + \hat{H}_x$, is a sum of Hamiltonians $\hat{H}_{h,\alpha}$ for each of the two horizontal legs $\alpha \in \{0, 1\}$ of the ladder, the vertical coupling between them, \hat{H}_v , and the cross-coupling \hat{H}_x present in experiment [39]. Specifically,

$$\begin{aligned} \hat{H}_{h,\alpha} &= J_h \sum_j [(-1)^{j+\alpha} \hat{\sigma}_{j,\alpha}^+ \hat{\sigma}_{j+1,\alpha}^- + \text{h.c.}], \\ \hat{H}_v &= J \sum_j (\hat{\sigma}_{j,\bar{\alpha}}^+ \hat{\sigma}_{j,\alpha}^- + \text{h.c.}), \\ \hat{H}_x &= \sum_\alpha \sum_j J_{x,j} (\hat{\sigma}_{j,\alpha}^+ \hat{\sigma}_{j+1,\bar{\alpha}}^- + \text{h.c.}), \end{aligned} \quad (2)$$

with $\hat{\sigma}_{j,\alpha}^\pm$ being the standard raising (lowering) spin-1/2 operators for j th spin in layer α , with $\bar{\alpha}$ denoting the layer opposite to α . The ladder contains $L = 2N$ spins in total. We assume open boundary conditions and set $J = 1$ as the overall energy scale. Note that we are allowing the cross-coupling $J_{x,j}$ to be site-dependent or even random.

When $J_{x,j} = 0$, the SCL model hosts exact QMBS eigenstates $|E_{n_s}\rangle$, which are simply the Dicke states of a free collective spin, $\hat{S}_0 = \sum_j \hat{\sigma}_j^x$ [87]. These eigenstates overlap with the product state $|\Pi\rangle = |\bullet\circ\circ\circ\cdots\rangle$, where “ \bullet ” and “ \circ ” denote the basis states of a single site. The state $|\Pi\rangle$ exhibits perfect revivals for $J_{x,j} = 0$. On the other hand, when $J_{x,j} \neq 0$, the QMBS eigenstates $|E_{n_s}\rangle$ are only approximately given by the Dicke states and the revivals acquire a decaying envelope [39]. In the Liouvillean spectrum, QMBS eigenmodes can be identified via the overlap with QMBS eigenmodes $|E_{n_s}\rangle \otimes |E_{m_s}\rangle$ at $\gamma=0$. When the dephasing becomes strong, one can only track the scar states by following smooth changes of the Liouville spectrum as γ is slowly varied.

Spectral transition in SCL model—In Fig. 1(b)-(d), we present examples of Liouvillean spectra of the SCL model in Eq. (2) with approximate QMBSs ($J_h = 0.66$, $J_{x,j} = 0.1$) at dephasing-free, small, and large pure dephasing rates, respectively. The QMBSs display distinct real Liouvillean eigenvalues. At weak dephasing $\gamma=0.0005$, those normalized eigenvalues featuring substantial displacement [red dots in panel (c)] cluster on the imaginary axis. In contrast, at the higher dephasing rate of $\gamma=0.02$ [panel (d)], the same eigenvalues exhibit a qualitatively different distribution pattern in the form of a sparse diamond grid. We also note that the right-most

eigenstates at larger dephasing rate, Fig. 1(d), have large overlap with the $|\Pi\rangle \otimes |\Pi\rangle$ state [87].

The stark difference between panels (c) and (d) of Fig. 1 reveals a shift of the eigenvalues along the real axis, which can be understood from the symmetry classification developed in Ref. [88]. The SCL Liouvillian obeys the $\mathbb{P}\mathbb{T}$ symmetry property, which is generated by the superoperator \mathcal{T}_- ,

$$\mathcal{T}_- = \sqrt{\pm 1} \left[\left(\prod_i \hat{\sigma}_i^x \right) \otimes \hat{I} \right] \mathcal{K}, \quad \mathcal{T}_- \mathcal{L} \mathcal{T}_-^{-1} = -\mathcal{L}, \quad (3)$$

where \mathcal{K} is the complex-conjugation superoperator. The existence of \mathcal{T}_- is responsible for D_2 dihedral symmetry of the QMBS Liouvillian spectrum in Fig. 1(c) [82]. At $\gamma = 0$, $|-(\lambda')^*\rangle$ degenerates with $|\lambda'\rangle$ and these lie on the imaginary axis. Beyond a certain γ , $\mathbb{P}\mathbb{T}|\lambda'\rangle = |-(\lambda')^*\rangle$ continues to hold, but λ' and $-(\lambda')^*$ are no longer the same. Thus, after this critical point, pairs of degenerate eigenvalues move symmetrically away from the imaginary axis along the real axis, resulting in LPTS breaking [82].

A few comments are in order. The LPTS breaking described above occurs only in inversion symmetry sector $p=\mp 1$, corresponding to odd or even N , respectively, see $N = 5$ case in Fig. 1(c). In contrast, the LPTS is already broken for infinitesimal γ in $p=\pm 1$ sector, also correlating with odd or even N . Moreover, the spectral features in Fig. 1 are exclusive to models with approximate QMBSs, while exact QMBSs break LPTS at infinitesimal γ . Intuitively, the latter is due to the exact energy spacing, which leads to the degeneracy of energy differences, $E_{n_s} - E_{m_s}$, on the imaginary axis. Hence, the Liouvillian eigenvalues of exact QMBSs jump into the complex plane for any $\gamma \neq 0$, as confirmed in the SM for $J_{x,j} = 0$ [87].

The process of LPTS breaking can be captured more quantitatively by sweeping the dephasing rate γ . Figures 2(a)-(b) illustrate the imaginary part of eigenvalues λ and the real part of normalized (shifted) eigenvalues λ'/γ as a function of γ . At weak dephasing, several eigenvalues with inversion symmetry $p=-1$ remain stationary along the real axis, while moving along the imaginary one. As γ increases, some pairs of eigenvalues collide on the imaginary axis and abruptly bifurcate into two branches at specific dephasing rates $\gamma_\star^{S(1,2,3)}$ along the real axis. These critical rates can be accurately estimated in a perturbation theory framework discussed below, whose prediction is shown in Fig. 2(c).

LPTS breaking can also be seen in the average movement velocity $\text{Re}(\bar{v}) = \text{Re}\langle d(\lambda'/\gamma)d\gamma \rangle$ as a function of γ in Fig. 2(d). For the $p=-1$ sector, a few distinct peaks align with the fast breaking velocities in Figs. 2(a)-(b) and the breaking points $\gamma_\star^{S(1,2,3)}$ correspond to the front of three peaks. There are no such abrupt peaks in $p=+1$ sector of QMBSs. In contrast, $\text{Re}(\bar{v})$ of thermal eigenvalues becomes smooth with increasing γ , implying no

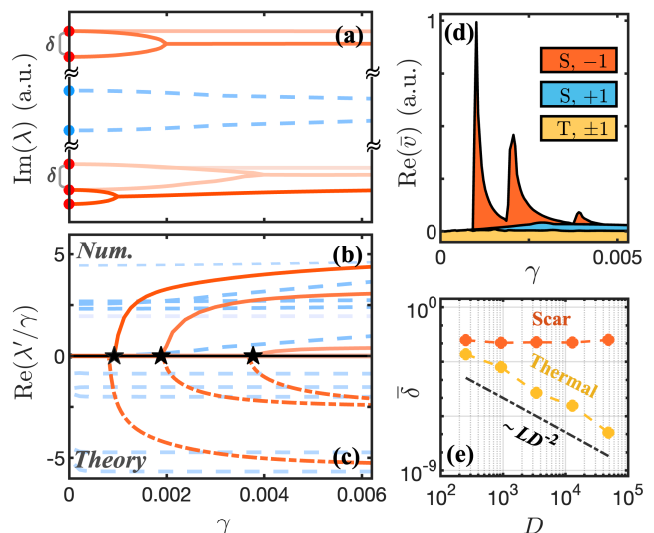


Figure 2. (a,b) The evolution of the Liouvillian spectrum, $\text{Im}(\lambda)$ and $\text{Re}(\lambda'/\gamma)$, as the dephasing rate γ is varied. The color intensity signifies the extent of real-axis difference. For improved visualization, the imaginary eigenvalues in panel (a) have been offset within a small window. Red and blue dots in (a) indicate the scarred eigenvalue spacings for the dephasing-free case. (c) Analytical prediction of LPTS breaking points $\gamma_\star^{S(1,2,3)}$ (black stars) based on perturbation theory are in good agreement with the numerical data (see text for details). (d) The average derivative $\text{Re}(\bar{v})$ as a function of the dephasing rate γ for QMBS and thermal states. (e) The average spacing $\bar{\delta}$ between the scarred and thermal eigenenergies in the dephasing-free case, plotted as a function of the Hilbert space dimension D . All data is for the SCL model with couplings $J_h = 0.66$, $J_{x,j} = 0.1$. Panels (a)-(d) are for system size $L = 10$ with open boundary conditions.

critical points.

LPTS breaking in perturbation theory—To understand the spectra in Fig. 2, we have developed a Liouvillian degenerate perturbation theory valid for small γ , see SM [87] for details. The Hamiltonian of the scar subspace can be rewritten as $\hat{S} = \hat{S}_0 + \hat{\Sigma}$, where $\hat{\Sigma}$ is the self-energy from the thermal subspace. If we neglect the coupling between the bath and the thermal subsystem, the Liouvillian of approximate QMBS is expressed as

$$\mathcal{S} \approx \mathcal{S}_0 + \mathcal{E} + \gamma_{\text{eff}} \mathcal{D}, \quad \mathcal{E} = -i(\hat{\Sigma} \otimes \hat{I} - \hat{I} \otimes \hat{\Sigma}), \quad (4)$$

where the self-energy superoperator \mathcal{E} is calculated using a non-equilibrium Green's function and γ_{eff} is model-dependent [87].

For the SCL model, the scar states are simply the Dicke states $|E_{n_s}\rangle$ of a free collective spin of magnitude $N/2$ [87]. The eigenmodes of the dephasing-free Liouvillian \mathcal{S}_0 are $|\lambda_{(l,s)}^{(0)}\rangle\rangle = |E_{l+s}\rangle \otimes |E_s\rangle$, corresponding to eigenvalues $\lambda_{(l,s)}^{(0)} = i(E_{l+s} - E_s) = 2il$ with indices $l = -N, -N+1, \dots, N-1, N$ and $s = 0, 1, 2, \dots, N-|l|$ labeling the states of the QMBS subspace. For clarifi-

cation, as illustrated in Fig. 1, the layer indices l are divided into two classes: l'' for the sector with LPTS breaking and l' for the sector without LPTS breaking. In first-order perturbation theory, the corrections to the traceless Liouvillian eigenvalues for the layer l are obtained by diagonalizing the projection of $(\mathcal{E} + \gamma_{\text{eff}}\mathcal{D}')$ to the degenerate subspace of the l th layer. For the finite-size SCL model in Fig. 2, the perturbed eigenvalues can be expressed in closed form [87], and we plot them against the numerical result in Fig. 2(c).

The analytical prediction of $\bar{\gamma}_*^{(1,2,3)}$ in perturbation theory aligns well with the numerical results [Figs. 2(b)-(c)], implying that LPTS breaking in QMBS Liouvillian spectra originates from the competition between dissipation $\gamma_{\text{eff}}\mathcal{D}'$ and the self-energy \mathcal{E} . Hence, we can estimate the LPTS breaking point for QMBS Liouvillian eigenvalues:

$$\bar{\gamma}_*^S \sim \|\mathcal{E}\| \times \|\mathcal{D}'\|^{-1} \sim L^{-1}, \quad (5)$$

which follows from the operator norm of \mathcal{D}' being extensive in system size, while $\|\hat{\Sigma}\|$ is a constant [87]. This estimate is consistent with Fig. 2(e), where we numerically extract the scaling behavior of the average spacing $\bar{\delta}$ for scar and thermal eigenvalues in the dephasing-free case ($\gamma = 0$) as a function of the Hilbert space dimension D . The typical spacing for thermal eigenvalues scales as $\bar{\delta} \sim LD^{-2}$, while the scar $\bar{\delta}^S$ is nearly independent of D . Then, the heuristic estimate of the typical LPTS breaking point, $\bar{\gamma}_*^S \sim \bar{\delta}^S \|\mathcal{D}'\|^{-1}$, is in agreement with Eq. (5). This is in stark contrast with the exponential scaling $\bar{\gamma}_* \sim D^{-2}$ of thermal eigenvalues [82]. Thus, while $\bar{\gamma}_*$ is prohibitively small for a generic many-body system, the presence of both QMBSs and \mathcal{T}_- symmetry gives rise to LPTS breaking points that scale polynomially with system size and have robust experimental signatures, as shown below.

Dynamical signatures—We demonstrate that weak dependence of $\bar{\gamma}_*^S$ on system size allows for QMBS signatures to persist in open-system dynamics. The time evolution is calculated from the Lindblad equation in the Markovian approximation as $d|\rho(t)\rangle\rangle/dt = \mathcal{L}|\rho(t)\rangle\rangle$ [85]. We integrate this equation starting from the initial state $|\rho(0)\rangle\rangle = |\rho_\Pi\rangle\rangle = |\Pi\rangle \otimes |\Pi\rangle$ and characterize its subsequent time evolution respectively by computing the fidelity and the density imbalance,

$$F(t) = |\langle\langle \rho_\Pi | \rho(t) \rangle\rangle| = \left| \sum_k \langle\langle \rho_\Pi | \lambda_k \rangle\rangle^2 e^{\lambda_k t} \right|, \quad (6)$$

$$I(t) = \frac{1}{L} \sum_j \langle\langle \hat{\sigma}_j^z \otimes \hat{\sigma}_j^z \rangle\rangle_0 \langle\langle \hat{\sigma}_j^z \otimes \hat{\sigma}_j^z \rangle\rangle_t,$$

where $\langle\langle \hat{\sigma}_j^z \otimes \hat{\sigma}_j^z \rangle\rangle_t = \langle\langle \rho(t) | \hat{\sigma}_j^z \otimes \hat{\sigma}_j^z | \rho(t) \rangle\rangle$. As the fidelity dynamics directly corresponds to the Liouvillian spectrum, the variance of fidelity density at the first revival point $\ln(F_1)/L$ can manifest the Liouvillian spectrum

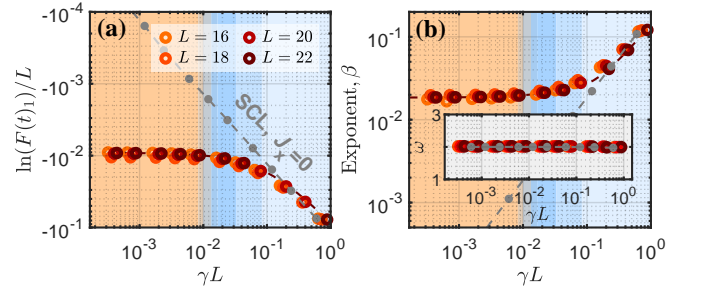


Figure 3. The global fidelity density at the first revival, $\ln(F_1)/L$, (a) and the decay coefficient β of density imbalance (b) for the SCL model as a function of dephasing γ . The orange and blue shaded areas represent before and after the LPTS breaking point $\bar{\gamma}_*^S$, respectively. For $\gamma < \bar{\gamma}_*^S$, both the fidelity density and imbalance decay are well-converged in system size, suggesting the robustness of scar signatures over a finite range of γL . By contrast, in the exact QMBS case with $J_{x,j} = 0$ (dashed line), the imbalance decay is highly sensitive to γ across the whole range. All data is for $J_h = 0.66$, $J_{x,j} \in [0, 0.2]$ drawn from a uniform distribution. Parameters (β, ω) are obtained by fitting the imbalance dynamics over the time period $[0, 3.2]$. These results are obtained by TEBD algorithm based on ITensor library [89].

transition. Furthermore, the imbalance dynamics takes the form of a damped oscillation, which can be fit using $I(t) = \exp(-\beta t) \cos(\omega t)$ over short time periods. In Fig. 3, $\ln(F_1)/L$ for the SCL model with dephasing is shown in panel (a), while the extracted imbalance parameters (ω, β) are plotted in panel (b). Below the LPTS breaking point, both quantities are well-converged and weakly depend on γ . For exact QMBSs with $J_{x,j} = 0$ in Fig. 3(b), the decay exponent β shows a power-law growth, while for approximate QMBS, β is nearly constant before the breaking point. As the dephasing rate further increases, the behavior of approximate and exact QMBSs become similar.

Conclusions—By analyzing the Liouvillian spectra and dynamics in the presence of dephasing, we demonstrated that QMBSs can undergo a dissipative transition that resembles LPTS breaking. This behavior distinguishes approximate QMBSs from thermal states; the former exhibit a certain degree of robustness to a dephasing dissipation, reminiscent of their behavior under closed system dynamics when prepared in a thermal Gibbs state [90]. We note that quantum noise is crucial for observing the QMBS LPTS breaking phenomena as the latter do not persist under a non-Hermitian Hamiltonian approximation [87].

We supported our conclusions using the SCL model realized in experiment [39]. In Appendix, we perform the same analysis for the PXP model of Rydberg atom arrays, finding a similar transition in its Liouvillian spectrum as a function of pure dephasing. While the PXP model lacks the \mathcal{T}_- symmetry [Eq. (3)], it displays similar (albeit approximate) LPTS breaking and similar ro-

bustness of QMBS signatures. Further evidence of LPTS breaking for the 1D tilted Fermi-Hubbard model [35], and ladder models with Hilbert space fragmentation [91] is presented in the SM [87]. The last example suggests that the phenomenon of spontaneous LPTS breaking may be a general feature of systems that weakly break ergodicity, extending beyond QMBSs. Furthermore, it remains unclear whether the stable dynamics present before the critical dephasing rate in systems beyond QMBSs. These deserve a more systematic investigation beyond the scope of the present work. Another open question concerns the effect of other types of dissipation on LPTS breaking and their underlying mechanisms. Finally, in closed systems, QMBSs have been proposed for quantum sensing [64], and it would be interesting to explore the sensitivity of such applications to dephasing noise.

Acknowledgments—We thank Profs. J.-S. Jin, Z.-W. Zhou, W.-G. Wang, X.-J. Liu, D.-L. Deng for helpful discussions. We also appreciate Dr. J. Ren discussion on TEBD simulation for quantum open systems. This work was supported by the Zhejiang Provincial Natural Science Foundation of China (No. LD25A050002), the National Natural Science Foundation of China (Nos. 12375021 and 12247101), the Fundamental Research Funds for the Central Universities (Grant No. lzujbky-2024-jdzz06), and the National Key Research and Development Program of China (No. 2022YFA1404203). Z.P. acknowledges support by the Leverhulme Trust Research Leadership Award RL-2019-015 and EPSRC Grant EP/Z533634/1. Statement of compliance with EPSRC policy framework on research data: This publication is theoretical work that does not require supporting research data. This research was supported in part by grant NSF PHY-2309135 to the Kavli Institute for Theoretical Physics (KITP).

Appendix: PXP Model

A paradigmatic example of approximate QMBSs is the PXP model that describes Rydberg atom arrays [14]. The PXP Hamiltonian is [92, 93]

$$\hat{H}_{\text{PXP}} = \Omega \sum_j^L \hat{P}_{j-1} \hat{\sigma}_j^x \hat{P}_{j+1}, \quad (7)$$

where $\hat{\sigma}_j^{x,y,z}$ are the Pauli matrices, $\hat{P}_j = (1 - \hat{\sigma}_j^z)/2$, and we set the Rabi frequency to $\Omega = 1$. The model features revival dynamics when the system is quenched from the initial state $|\mathbb{Z}_2\rangle \equiv |\uparrow\downarrow\uparrow\downarrow\cdots\rangle$ [15, 94]. Below we demonstrate that the PXP model with pure dephasing exhibits similar behavior to the SCL model.

Figures 4(a)-(c) illustrate the Liouvillean spectra for the PXP model for several dephasing rates. These results are qualitatively similar to the SCL model in Fig. 2: for weak dephasing $\gamma = 0.0004$, the scar eigenvalues cluster

around $\text{Re}(\lambda') = 0$, while at larger dephasing, $\gamma = 0.04$, these eigenvalues pair-wisely shift to both sides along the real axis. The main difference is that the PXP model does not possess the \mathcal{T}_- symmetry in Eq. (3). Hence, its Liouvillean spectrum, even at small $\gamma = 0.0004$, does not have an exact D_2 symmetry and LPTS, strictly speaking, is already broken at that point. However, the clustering of the scar eigenvalues around the imaginary and real axes at small γ suggests that their movement is largely similar to the SCL model. We next show that scar eigenvalues of the PXP Liouvillean indeed undergo sharp jumps upon sweeping the dephasing rate, similar to the SCL model.

Figures 4(d) and (e) illustrate the imaginary part of eigenvalues and real part of normalized eigenvalues λ'/γ as a function of γ . Several eigenvalues with momentum $q = 0$ remain stationary at weak dephasing, while some pairs of eigenvalues abruptly bifurcate into two branches at specific dephasing rates $\lambda_\star^{(1,2,3)}$. In contrast, no such LPTS breakings occur in the momentum sector $q = \pi$. The LPTS breaking can be seen in the average movement velocity $\text{Re}(v)$ as a function of γ in Fig. 4(f). For the $q = 0$ momentum sector of the PXP model, a few distinct peaks align with the fast breaking velocities in Figs. 4(d)-(e) and the breaking points $\gamma_\star^{(1,2,3)}$ correspond to the front of three peaks. There are no such abrupt peaks in $q = \pi$ sector of QMBSs. Moreover, the average movement velocity of thermal eigenvalues become more stable with increasing γ , implying no critical points.

The typical LPTS breaking point $\bar{\gamma}_\star^S$ for PXP scar eigenmodes can be estimated from the spacings $\bar{\delta}$ of non-degenerate scar eigenvalues at $\gamma = 0$ according to the same expression, $\bar{\gamma}_\star^S \sim \bar{\delta} \|\mathcal{D}'\|^{-1}$, used previously for the SCL model in the main text. As confirmed in the inset of Fig. 4(a), $\bar{\delta} \sim LD^{-2}$ for thermal eigenvalues, while the scar $\bar{\delta}$ is nearly independent of D . Thus, the typical critical point for PXP scar eigenmodes also scales as $\bar{\gamma}_\star^S \sim L^{-1}$, consistent with the approximate QMBSs in the SCL model.

Similar to the SCL model in the main text, we check for the robustness of scar signatures in the dynamics by performing the time evolution generated by the Lindblad equation for the PXP model with pure dephasing. Here we take as initial state $|\rho_{\mathbb{Z}_2}\rangle\rangle = |\mathbb{Z}_2\rangle \otimes |\mathbb{Z}_2\rangle$ and the resulting fidelity density at the first revival, $\ln F_1/L$, as well as the imbalance decay β and frequency ω , are shown in Fig. 5. These results mirror those for the SCL model, in particular β has a similarly weak dependence on γ as long as $\gamma < \gamma_\star^S$.

To confirm that these results are due to approximate QMBSs, we consider a deformation of the PXP model [17, 19, 63] for which QMBSs assume a nearly ex-

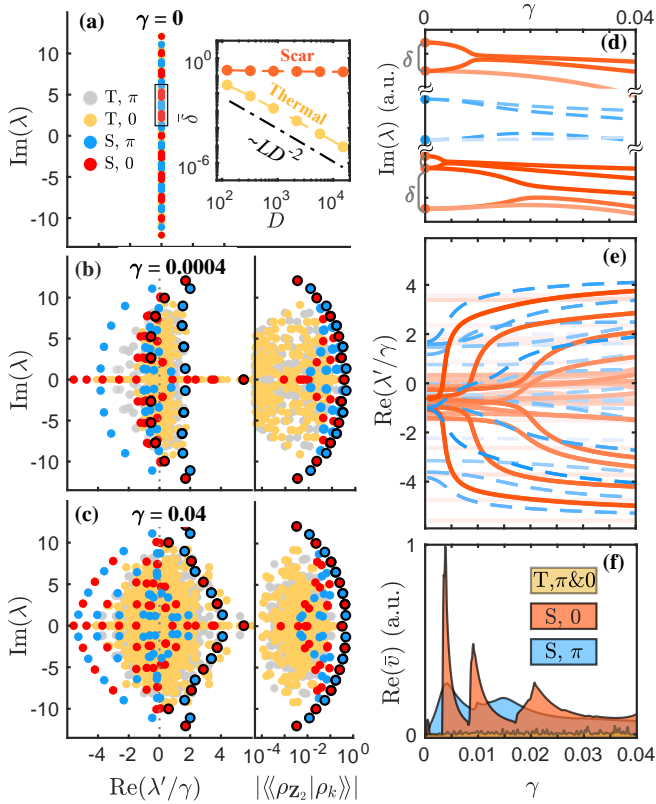


Figure 4. (a-c) The Liouvillean eigenspectra of the PXP model for dephasing strengths $\gamma = 0, 0.0004, 0.04$. Red and blue dots represent scar (S) eigenvalues, while yellow and gray ones represent thermal (T) eigenvalues. These are further classified by momenta $q = 0$ and π under translations. The inset in (a) shows the average scar eigenvalue spacing, $\bar{\delta}$, at zero dephasing, plotted as a function of the corresponding sector dimension D . The right panels in (b)-(c) show the overlaps of Liouvillean eigenmodes with $|\mathbb{Z}_2\rangle \otimes |\mathbb{Z}_2\rangle$ state, with black circles highlighting local maxima. (d)-(e) The evolution of the Liouvillean spectrum, $\text{Im}(\lambda)$ and $\text{Re}(\lambda'/\gamma)$, as the dephasing rate γ is varied. The color intensity signifies the extent of real-axis difference. For improved visualization, the imaginary values in panel (d) have been shifted within a small window. Red dots indicate the scarred eigenvalue spacings for the dephasing-free case. (f) The average derivative $\text{Re}(\bar{\nu})$ as a function of the dephasing rate γ for the QMBs and the thermal states. All data is obtained by exact diagonalization of the PXP model for a system size of $L = 10$ and with periodic boundary conditions.

act form:

$$\hat{H}_{\text{DPXP}} = \hat{H}_{\text{PXP}} + \sum_j^L \sum_{d=2}^{L/2} J_d \hat{P}_{j-1} \hat{\sigma}_j^x \hat{P}_{j+1} (\hat{\sigma}_{j-d}^z + \hat{\sigma}_{j+d}^z). \quad (8)$$

At the optimal coupling strength $J_d = 0.051(\phi^{d-1} + \phi^{1-d})^{-2}$, with $\phi = (1 + \sqrt{5})/2$, the QMBS subspace contains $L+1$ eigenstates that are almost perfectly decoupled from the thermal bulk of the spectrum [17]. This DPXP model indeed behaves similarly to the exact QMBs in

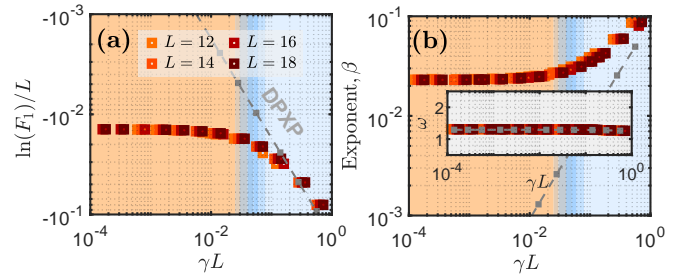


Figure 5. The global fidelity density at the first revival, $\ln(F_1)/L$ (a) and the decay coefficient β of density imbalance (b) for the PXP model as a function of dephasing γ . The orange and blue areas represent before and after the LPTS breaking point γ_*^S , respectively. Parameters (β, ω) are obtained by fitting the imbalance dynamics over the time period $[0, 10]$. These results are obtained by exact diagonalization.

the SCL model with $J_{x,j} = 0$, e.g., the imbalance decay coefficient β exhibits a similar power-law dependence on γ in both cases. The similarity extends to the Liouvillean spectra, as the DPXP model also exhibits LPTS breaking for infinitesimal γ , see SM [87].

* These authors contributed equally

† z.papic@leeds.ac.uk

‡ leiying@zju.edu.cn

- [1] I. Bloch, J. Dalibard, and S. Nascimbène, Quantum simulations with ultracold quantum gases, *Nat. Phys.* **8**, 267 (2012).
- [2] I. M. Georgescu, S. Ashhab, and F. Nori, Quantum simulation, *Rev. Mod. Phys.* **86**, 153 (2014).
- [3] M. Kjaergaard, M. E. Schwartz, J. Braumüller, P. Krantz, J. I.-J. Wang, S. Gustavsson, and W. D. Oliver, Superconducting qubits: Current state of play, *Annual Review of Condensed Matter Physics* **11**, 369 (2020).
- [4] A. Browaeys and T. Lahaye, Many-body physics with individually controlled Rydberg atoms, *Nat. Phys.* **16**, 132 (2020).
- [5] C. Monroe, W. C. Campbell, L.-M. Duan, Z.-X. Gong, A. V. Gorshkov, P. W. Hess, R. Islam, K. Kim, N. M. Linke, G. Pagano, P. Richerme, C. Senko, and N. Y. Yao, Programmable quantum simulations of spin systems with trapped ions, *Rev. Mod. Phys.* **93**, 025001 (2021).
- [6] J. M. Deutsch, Quantum statistical mechanics in a closed system, *Phys. Rev. A* **43**, 2046 (1991).
- [7] M. Srednicki, Chaos and quantum thermalization, *Phys. Rev. E* **50**, 888 (1994).
- [8] M. Rigol, V. Dunjko, and M. Olshanii, Thermalization and its mechanism for generic isolated quantum systems, *Nature* **452**, 854 (2008).
- [9] L. D'Alessio, Y. Kafri, A. Polkovnikov, and M. Rigol, From quantum chaos and eigenstate thermalization to statistical mechanics and thermodynamics, *Adv. Phys.* **65**, 239 (2016).
- [10] M. Ueda, Quantum equilibration, thermalization and prethermalization in ultracold atoms, *Nature Reviews*

- Physics* **2**, 669 (2020).
- [11] M. Serbyn, D. A. Abanin, and Z. Papić, Quantum many-body scars and weak breaking of ergodicity, *Nature Physics* **17**, 675 (2021).
- [12] S. Moudgalya, B. A. Bernevig, and N. Regnault, Quantum many-body scars and hilbert space fragmentation: a review of exact results, *Reports on Progress in Physics* **85**, 086501 (2022).
- [13] A. Chandran, T. Iadecola, V. Khemani, and R. Moessner, Quantum many-body scars: A quasiparticle perspective, *Annual Review of Condensed Matter Physics* **14**, 443 (2023).
- [14] H. Bernien, S. Schwartz, A. Keesling, H. Levine, A. Omran, H. Pichler, S. Choi, A. S. Zibrov, M. Endres, M. Greiner, *et al.*, Probing many-body dynamics on a 51-atom quantum simulator, *Nature* **551**, 579 (2017).
- [15] C. J. Turner, A. A. Michailidis, D. A. Abanin, M. Serbyn, and Z. Papić, Weak ergodicity breaking from quantum many-body scars, *Nature Physics* **14**, 745 (2018).
- [16] W. W. Ho, S. Choi, H. Pichler, and M. D. Lukin, Periodic orbits, entanglement, and quantum many-body scars in constrained models: Matrix product state approach, *Phys. Rev. Lett.* **122**, 040603 (2019).
- [17] S. Choi, C. J. Turner, H. Pichler, W. W. Ho, A. A. Michailidis, Z. Papić, M. Serbyn, M. D. Lukin, and D. A. Abanin, Emergent su(2) dynamics and perfect quantum many-body scars, *Phys. Rev. Lett.* **122**, 220603 (2019).
- [18] F. M. Surace, P. P. Mazza, G. Giudici, A. Lerose, A. Gambassi, and M. Dalmonte, Lattice gauge theories and string dynamics in Rydberg atom quantum simulators, *Phys. Rev. X* **10**, 021041 (2020).
- [19] V. Khemani, C. R. Laumann, and A. Chandran, Signatures of integrability in the dynamics of Rydberg-blockaded chains, *Phys. Rev. B* **99**, 161101 (2019).
- [20] C.-J. Lin and O. I. Motrunich, Exact quantum many-body scar states in the rydberg-blockaded atom chain, *Phys. Rev. Lett.* **122**, 173401 (2019).
- [21] C.-J. Lin, V. Calvera, and T. H. Hsieh, Quantum many-body scar states in two-dimensional rydberg atom arrays, *Phys. Rev. B* **101**, 220304 (2020).
- [22] D. Bluvstein, A. Omran, H. Levine, A. Keesling, G. Semeghini, S. Ebadi, T. T. Wang, A. A. Michailidis, N. Maskara, W. W. Ho, S. Choi, M. Serbyn, M. Greiner, V. Vuletić, and M. D. Lukin, Controlling quantum many-body dynamics in driven rydberg atom arrays, *Science* **371**, 1355 (2021).
- [23] I. Mondragon-Shem, M. G. Vavilov, and I. Martin, Fate of quantum many-body scars in the presence of disorder, *PRX Quantum* **2**, 030349 (2021).
- [24] K. Omiya and M. Müller, Quantum many-body scars in bipartite rydberg arrays originating from hidden projector embedding, *Phys. Rev. A* **107**, 023318 (2023).
- [25] L. Zhao, P. R. Datla, W. Tian, M. M. Aliyu, and H. Loh, Observation of quantum thermalization restricted to hilbert space fragments and F_{2k} scars, *Phys. Rev. X* **15**, 011035 (2025).
- [26] A. Kerschbaumer, M. Ljubotina, M. Serbyn, and J.-Y. Desaulles, Quantum many-body scars beyond the pxp model in rydberg simulators (2024), [arXiv:2410.18913 \[quant-ph\]](https://arxiv.org/abs/2410.18913).
- [27] D. Ding, Z. Bai, Z. Liu, B. Shi, G. Guo, W. Li, and C. S. Adams, Ergodicity breaking from rydberg clusters in a driven-dissipative many-body system, *Science Advances* **10**, ead15893 (2024).
- [28] A. N. Ivanov and O. I. Motrunich, Many exact area-law scar eigenstates in the nonintegrable pxp and related models (2025), [arXiv:2503.16327 \[quant-ph\]](https://arxiv.org/abs/2503.16327).
- [29] S. Moudgalya, N. Regnault, and B. A. Bernevig, Entanglement of exact excited states of affleck-kennedy-lieb-tasaki models: Exact results, many-body scars, and violation of the strong eigenstate thermalization hypothesis, *Phys. Rev. B* **98**, 235156 (2018).
- [30] M. Schecter and T. Iadecola, Weak ergodicity breaking and quantum many-body scars in spin-1 xy magnets, *Phys. Rev. Lett.* **123**, 147201 (2019).
- [31] K. Yang, Y. Zhang, K.-Y. Li, K.-Y. Lin, S. Gopalakrishnan, M. Rigol, and B. L. Lev, Phantom energy in the nonlinear response of a quantum many-body scar state, *Science* **385**, 1063 (2024).
- [32] Z. Guo, B. Liu, Y. Gao, A. Yang, J. Wang, J. Ma, and L. Ying, Origin of hilbert-space quantum scars in unconstrained models, *Phys. Rev. B* **108**, 075124 (2023).
- [33] A. Hudomal, I. Vasić, N. Regnault, and Z. Papić, Quantum scars of bosons with correlated hopping, *Communications Physics* **3**, 99 (2020).
- [34] H. Zhao, J. Vovrosh, F. Mintert, and J. Knolle, Quantum many-body scars in optical lattices, *Phys. Rev. Lett.* **124**, 160604 (2020).
- [35] J.-Y. Desaulles, A. Hudomal, C. J. Turner, and Z. Papić, Proposal for realizing quantum scars in the tilted 1d fermi-hubbard model, *Phys. Rev. Lett.* **126**, 210601 (2021).
- [36] S. Scherg, T. Kohlert, P. Sala, F. Pollmann, B. Hebbe Madhusudhana, I. Bloch, and M. Aidelsburger, Observing non-ergodicity due to kinetic constraints in tilted fermi-hubbard chains, *Nature Communications* **12**, 4490 (2021).
- [37] G.-X. Su, H. Sun, A. Hudomal, J.-Y. Desaulles, Z.-Y. Zhou, B. Yang, J. C. Halimeh, Z.-S. Yuan, Z. Papić, and J.-W. Pan, Observation of many-body scarring in a Bose-Hubbard quantum simulator, *Phys. Rev. Res.* **5**, 023010 (2023).
- [38] D. Adler, D. Wei, M. Will, K. Srakaew, S. Agrawal, P. Weckesser, R. Moessner, F. Pollmann, I. Bloch, and J. Zeiher, Observation of hilbert space fragmentation and fractonic excitations in 2d, *Nature* **636**, 80 (2024).
- [39] P. Zhang, H. Dong, Y. Gao, L. Zhao, J. Hao, J.-Y. Desaulles, Q. Guo, J. Chen, J. Deng, B. Liu, *et al.*, Many-body hilbert space scarring on a superconducting processor, *Nature Physics* **19**, 120 (2023).
- [40] P. G. Larsen, A. E. B. Nielsen, A. Eckardt, and F. Petziol, Experimental protocol for observing single quantum many-body scars with transmon qubits (2024), [arXiv:2410.14613 \[quant-ph\]](https://arxiv.org/abs/2410.14613).
- [41] N. Shiraishi and T. Mori, Systematic construction of counterexamples to the eigenstate thermalization hypothesis, *Phys. Rev. Lett.* **119**, 030601 (2017).
- [42] S. Ok, K. Choo, C. Mudry, C. Castelnovo, C. Chamon, and T. Neupert, Topological many-body scar states in dimensions one, two, and three, *Phys. Rev. Research* **1**, 033144 (2019).
- [43] N. Shibata, N. Yoshioka, and H. Katsura, Onsager's scars in disordered spin chains, *Phys. Rev. Lett.* **124**, 180604 (2020).
- [44] P. A. McClarty, M. Haque, A. Sen, and J. Richter, Disorder-free localization and many-body quantum scars from magnetic frustration, *Phys. Rev. B* **102**, 224303 (2020).

- [45] K. Lee, R. Melendrez, A. Pal, and H. J. Changlani, Exact three-colored quantum scars from geometric frustration, *Phys. Rev. B* **101**, 241111 (2020).
- [46] K. Pakrouski, P. N. Pallegar, F. K. Popov, and I. R. Klebanov, Many-body scars as a group invariant sector of hilbert space, *Phys. Rev. Lett.* **125**, 230602 (2020).
- [47] D. K. Mark and O. I. Motrunich, η -pairing states as true scars in an extended hubbard model, *Phys. Rev. B* **102**, 075132 (2020).
- [48] J. Ren, C. Liang, and C. Fang, Quasisymmetry groups and many-body scar dynamics, *Phys. Rev. Lett.* **126**, 120604 (2021).
- [49] S. Mohapatra and A. C. Balram, Pronounced quantum many-body scars in the one-dimensional spin-1 kitaev model, *Phys. Rev. B* **107**, 235121 (2023).
- [50] P. Kolb and K. Pakrouski, Stability of the many-body scars in fermionic spin-1/2 models, *PRX Quantum* **4**, 040348 (2023).
- [51] N. S. Srivatsa, H. Yarloo, R. Moessner, and A. E. B. Nielsen, Mobility edges through inverted quantum many-body scarring, *Phys. Rev. B* **108**, L100202 (2023).
- [52] J.-Y. Desaulles, D. Banerjee, A. Hudomal, Z. Papić, A. Sen, and J. C. Halimeh, Weak ergodicity breaking in the schwinger model, *Phys. Rev. B* **107**, L201105 (2023).
- [53] J. C. Halimeh, L. Barbiero, P. Hauke, F. Grusdt, and A. Bohrdt, Robust quantum many-body scars in lattice gauge theories, *Quantum* **7**, 1004 (2023).
- [54] B. Buča, Unified theory of local quantum many-body dynamics: Eigenoperator thermalization theorems, *Phys. Rev. X* **13**, 031013 (2023).
- [55] L. Gotta, S. Moudgalya, and L. Mazza, Asymptotic quantum many-body scars, *Phys. Rev. Lett.* **131**, 190401 (2023).
- [56] S. Moudgalya and O. I. Motrunich, Exhaustive characterization of quantum many-body scars using commutant algebras, *Phys. Rev. X* **14**, 041069 (2024).
- [57] B. Evrard, A. Pizzi, S. I. Mistakidis, and C. B. Dag, Quantum scars and regular eigenstates in a chaotic spinor condensate, *Phys. Rev. Lett.* **132**, 020401 (2024).
- [58] L. Logarić, S. Dooley, S. Pappalardi, and J. Goold, Quantum many-body scars in dual-unitary circuits, *Phys. Rev. Lett.* **132**, 010401 (2024).
- [59] A. Pizzi, B. Evrard, C. B. Dag, and J. Knolle, *Quantum scars in many-body systems* (2024), [arXiv:2408.10301](https://arxiv.org/abs/2408.10301) [quant-ph].
- [60] S. Moudgalya, N. Regnault, and B. A. Bernevig, η -pairing in hubbard models: From spectrum generating algebras to quantum many-body scars, *Phys. Rev. B* **102**, 085140 (2020).
- [61] D. K. Mark, C.-J. Lin, and O. I. Motrunich, Unified structure for exact towers of scar states in the affleck-kennedy-lieb-tasaki and other models, *Phys. Rev. B* **101**, 195131 (2020).
- [62] N. O’Dea, F. Burnell, A. Chandran, and V. Khemani, From tunnels to towers: Quantum scars from lie algebras and q -deformed lie algebras, *Phys. Rev. Res.* **2**, 043305 (2020).
- [63] K. Bull, J.-Y. Desaulles, and Z. Papić, Quantum scars as embeddings of weakly broken Lie algebra representations, *Phys. Rev. B* **101**, 165139 (2020).
- [64] S. Dooley, Robust quantum sensing in strongly interacting systems with many-body scars, *PRX Quantum* **2**, 020330 (2021).
- [65] J.-Y. Desaulles, F. Pietracaprina, Z. Papić, J. Goold, and S. Pappalardi, Extensive multipartite entanglement from $su(2)$ quantum many-body scars, *Phys. Rev. Lett.* **129**, 020601 (2022).
- [66] S. Dooley, S. Pappalardi, and J. Goold, Entanglement enhanced metrology with quantum many-body scars, *Phys. Rev. B* **107**, 035123 (2023).
- [67] A. Omran, H. Levine, A. Keesling, G. Semeghini, T. T. Wang, S. Ebadi, H. Bernien, A. S. Zibrov, H. Pichler, S. Choi, J. Cui, M. Rossignolo, P. Rembold, S. Montangero, T. Calarco, M. Endres, M. Greiner, V. Vuletić, and M. D. Lukin, Generation and manipulation of schrödinger cat states in rydberg atom arrays, *Science* **365**, 570 (2019).
- [68] H. Dong, J.-Y. Desaulles, Y. Gao, N. Wang, Z. Guo, J. Chen, Y. Zou, F. Jin, X. Zhu, P. Zhang, H. Li, Z. Wang, Q. Guo, J. Zhang, L. Ying, and Z. Papić, Disorder-tunable entanglement at infinite temperature, *Science Advances* **9**, eadj3822 (2023).
- [69] T. Albash and D. A. Lidar, Decoherence in adiabatic quantum computation, *Phys. Rev. A* **91**, 062320 (2015).
- [70] Y. Yao, L. Xiang, Z. Guo, Z. Bao, Y.-F. Yang, Z. Song, H. Shi, X. Zhu, F. Jin, J. Chen, S. Xu, Z. Zhu, F. Shen, N. Wang, C. Zhang, Y. Wu, Y. Zou, P. Zhang, H. Li, Z. Wang, C. Song, C. Cheng, R. Mondaini, H. Wang, J. Q. You, S.-Y. Zhu, L. Ying, and Q. Guo, Observation of many-body fock space dynamics in two dimensions, *Nature Physics* **19**, 1459 (2023).
- [71] B. Olmos, I. Lesanovsky, and J. P. Garrahan, Facilitated spin models of dissipative quantum glasses, *Phys. Rev. Lett.* **109**, 020403 (2012).
- [72] K. Macieszczak, M. Guță, I. Lesanovsky, and J. P. Garrahan, Towards a theory of metastability in open quantum dynamics, *Physical review letters* **116**, 240404 (2016).
- [73] B. Buča, J. Tindall, and D. Jaksch, Non-stationary coherent quantum many-body dynamics through dissipation, *Nature Communications* **10**, 1730 (2019).
- [74] C. Booker, B. Buča, and D. Jaksch, Non-stationarity and dissipative time crystals: spectral properties and finite-size effects, *New Journal of Physics* **22**, 085007 (2020).
- [75] F. M. Gambetta, F. Carollo, M. Marcuzzi, J. P. Garrahan, and I. Lesanovsky, Discrete time crystals in the absence of manifest symmetries or disorder in open quantum systems, *Phys. Rev. Lett.* **122**, 015701 (2019).
- [76] H. Keßler, P. Kongkhambut, C. Georges, L. Mathey, J. G. Cosme, and A. Hemmerich, Observation of a dissipative time crystal, *Phys. Rev. Lett.* **127**, 043602 (2021).
- [77] H.-R. Wang, D. Yuan, S.-Y. Zhang, Z. Wang, D.-L. Deng, and L.-M. Duan, Embedding quantum many-body scars into decoherence-free subspaces, *Phys. Rev. Lett.* **132**, 150401 (2024).
- [78] X.-P. Jiang, M. Xu, X. Yang, H. Hou, Y. Wang, and L. Pan, *Robustness of quantum many-body scars in the presence of markovian bath* (2025), [arXiv:2501.00886](https://arxiv.org/abs/2501.00886) [cond-mat.dis-nn].
- [79] A. M. García-García, Z. Lu, L. Sá, and J. J. M. Verbaarschot, *Lindblad many-body scars* (2025), [arXiv:2503.06665](https://arxiv.org/abs/2503.06665) [quant-ph].
- [80] C.-J. Lin, A. Chandran, and O. I. Motrunich, Slow thermalization of exact quantum many-body scar states under perturbations, *Phys. Rev. Res.* **2**, 033044 (2020).
- [81] F. M. Surace, M. Votto, E. G. Lazo, A. Silva, M. Dalmonde, and G. Giudici, Exact many-body scars and their stability in constrained quantum chains, *Phys. Rev. B* **103**, 104302 (2021).

- [82] T. Prosen, $\mathbb{P}T$ -symmetric quantum liouvillean dynamics, *Phys. Rev. Lett.* **109**, 090404 (2012).
- [83] Q. Chen, S. A. Chen, and Z. Zhu, Weak ergodicity breaking in non-Hermitian many-body systems, *SciPost Phys.* **15**, 052 (2023).
- [84] R. Shen, F. Qin, J.-Y. Desaulles, Z. Papić, and C. H. Lee, Enhanced many-body quantum scars from the non-hermitian fock skin effect, *Phys. Rev. Lett.* **133**, 216601 (2024).
- [85] H.-P. Breuer and F. Petruccione, *The theory of open quantum systems* (Oxford University Press, USA, 2002).
- [86] T. Iadecola and M. Žnidarič, Exact localized and ballistic eigenstates in disordered chaotic spin ladders and the fermi-hubbard model, *Phys. Rev. Lett.* **123**, 036403 (2019).
- [87] See the Supplemental Material for details of the derivations and results for other models.
- [88] L. Sá, P. Ribeiro, and T. c. v. Prosen, Symmetry classification of many-body lindbladians: Tenfold way and beyond, *Phys. Rev. X* **13**, 031019 (2023).
- [89] M. Fishman, S. R. White, and E. M. Stoudenmire, The ITensor Software Library for Tensor Network Calculations, *SciPost Phys. Codebases*, 4 (2022).
- [90] J.-Y. Desaulles, E. J. Gustafson, A. C. Y. Li, Z. Papić, and J. C. Halimeh, Robust finite-temperature many-body scarring on a quantum computer, *Phys. Rev. A* **110**, 042606 (2024).
- [91] D. Hahn, P. A. McClarty, and D. J. Luitz, Information dynamics in a model with Hilbert space fragmentation, *SciPost Phys.* **11**, 074 (2021).
- [92] P. Fendley, K. Sengupta, and S. Sachdev, Competing density-wave orders in a one-dimensional hard-boson model, *Phys. Rev. B* **69**, 075106 (2004).
- [93] I. Lesanovsky and H. Katsura, Interacting Fibonacci anyons in a Rydberg gas, *Phys. Rev. A* **86**, 041601(R) (2012).
- [94] C. J. Turner, A. A. Michailidis, D. A. Abanin, M. Serbyn, and Z. Papić, Quantum scarred eigenstates in a Rydberg atom chain: Entanglement, breakdown of thermalization, and stability to perturbations, *Phys. Rev. B* **98**, 155134 (2018).

Supplementary Materials for “Liouvillean Spectral Transition in Noisy Quantum Many-Body Scars”

Jin-Lou Ma, Zexian Guo, Yu Gao, Zlatko Papić, and Lei Ying

A. Liouvillean perturbation theory

We focus on a class of quantum many-body scar (QMBS) systems whose Hamiltonian can be written as

$$\hat{H} = \hat{S}_0 \oplus \hat{T} + \hat{V}, \quad (\text{S1})$$

where \hat{S}_0 and \hat{T} denote the Hamiltonian of scar and thermal subsystems, respectively, while \hat{V} represents the coupling between them. This general Hamiltonian includes a large class of QMBS models [11]. For concreteness, here we will focus on the spin Creutz-ladder (SCL) model introduced in the main text, where \hat{S}_0 takes the form of a free paramagnet Hamiltonian, to be specified below.

The effect of the thermal subspace \hat{T} can be incorporated by defining the effective Hamiltonian for the QMBS subspace as $\hat{S} = \hat{S}_0 + \hat{\Sigma}$, where $\hat{\Sigma}$ is the self-energy from the thermal subspace. If we neglect the coupling between the bath and the thermal subsystem, the resulting Liouvillean can be written as

$$\mathcal{S} \approx \mathcal{S}_0 + \mathcal{E} + \gamma_{\text{eff}} \mathcal{D}. \quad (\text{S2})$$

Here, the Liouvillean of the exact scar subspace is denoted by \mathcal{S}_0 , while the self-energy and dissipator are

$$\mathcal{E} = -i(\hat{\Sigma} \otimes \hat{I} - \hat{I} \otimes \hat{\Sigma}), \quad \mathcal{D} = \mathcal{D}' - \sum_j \hat{I}_j \otimes \hat{I}_j, \quad \mathcal{D}' = \sum_j \hat{\sigma}_j^z \otimes \hat{\sigma}_j^z. \quad (\text{S3})$$

The self-energy can be obtained via the non-equilibrium Green's function as shown below. When \mathcal{E} is zero, the problem reduces to the exact scar case. The effective dephasing strength, γ_{eff} , is model-dependent. For example, in the SCL model, two neighboring sites in the real space are used to define a ‘spin’ in the scar subspace (i.e., $N = L/2$), thus we have $\gamma_{\text{eff}} = 2\gamma$.

In the SCL model, the QMBS Hamiltonian and its eigenstates are given by the Dicke states of a free collective spin of magnitude $N/2$:

$$\hat{S}_0 = J \sum_j \hat{\sigma}_j^x, \quad |E_{n_S}\rangle = \binom{N}{n_S}^{-\frac{1}{2}} \sum_{i_1 \neq \dots \neq i_{n_S}} \bigotimes_{j=1}^N \begin{cases} |+\rangle & j \in \{i_1, \dots, i_{n_S}\} \\ |-\rangle & \text{otherwise} \end{cases}, \quad (\text{S4})$$

where $|\pm\rangle_j = (|0\rangle_j \pm |1\rangle_j)/\sqrt{2}$ are the eigenvectors of a local $\hat{\sigma}_j^x$, and $n_S = 0, 1, \dots, N$ is the number of $|+\rangle$ appearing in the tensor product. We have written the eigenstates belonging to the maximal spin representation. The dephasing-free Liouvillean of the exact scar subspace is given by

$$\mathcal{S}_0 = -iJ \left(\sum_j \hat{\sigma}_j^x \otimes \hat{I} - \hat{I} \otimes \sum_j \hat{\sigma}_j^x \right), \quad (\text{S5})$$

with the corresponding eigenmodes and eigenvalues

$$|\lambda_{(l,s)}^{(0)}\rangle\rangle = |E_{l+s}\rangle \otimes |E_s\rangle, \quad \lambda_l^{(0)} = i(E_{l+s} - E_s) = 2ilJ. \quad (\text{S6})$$

The eigenmodes are labeled using indices $l = -N, -N+1, \dots, N$ and $s = 0, 1, 2, \dots, N-|l|$. The layer indices can be split into two groups, i.e. $\{l\} = \{l', l''\}$, where QMBS layers $l'' = -N, -N+2, \dots, N$ represent layers with spontaneous LPTS breaking process and $l' = -N+1, -N+3, \dots, N-1$ are the remaining layers.

A few comments are in order. The layers $l'' = \pm N$ are special in that they contain a single level $s = 0$. Consequently, as we show in Sec. A2 below, these QMBS Liouvillean eigenvalues remain on the imaginary axis for arbitrary values of the dephasing, while the other l'' sectors generally undergo LPTS breaking. Second, we note that our labeling of QMBS layers is unrelated with inversion symmetry quantum number. The latter is given by $p = (-1)^l$, therefore the LPTS-breaking states are found in different inversion-symmetric subspaces depending on the parity of N .

A1. Self-energy due to the thermal subspace

The Hamiltonian in Eq. (S1) is generally non-integrable and impossible to solve exactly. Hence we employ the non-equilibrium Green's function approach to model the effect of thermal bulk on the QMBS subspace, see Ref. [32] for details. This will allow us to obtain analytical insights into the interplay of scarring with the dephasing dissipation. The Green's function of the scar subspace is expressed as

$$\hat{G}_S(E) = \left[(E + i0^+) \hat{I} - \hat{S}_0 - \hat{\Sigma}(E) \right]^{-1}. \quad (\text{S7})$$

The self-energy is obtained by solving the self-consistent Dyson's equation:

$$\hat{\Sigma}(E) = \hat{\Gamma}^\dagger [E\hat{I} - \hat{S}_0 - \hat{\Sigma}(E)]^{-1} \hat{\Gamma}, \quad (\text{S8})$$

where $\hat{\Sigma}(E) = \sum_{p_S} \hat{\sigma}_{p_S}(E)$ represents the self-energy matrix, with $\hat{\sigma}_{p_S}(E) = \hat{\Gamma}_{p_S}^\dagger \hat{G}_0(E) \hat{\Gamma}_{p_S}$ and $\hat{\Gamma}_{p_S} = \sqrt{\gamma_{p_S}} |p_S\rangle \langle p_S|$. Here, $|p_S\rangle$ denote the product states in the scar subspace, and γ_{p_S} represents the interaction strength between the $|p_S\rangle$ and the thermal subspace. For the QMBS model we consider here, Eq. (S1), \hat{S}_0 corresponds to a hypercube and $|p_S\rangle$ represent some of the computational basis states, while the remaining basis states $|p_T\rangle$ span the thermal subspace. For example, in the SCL model the vertices of the hypercube are product states of dimers, $\{|p_S\rangle\} = \{\otimes_{j=1}^{N=L/2} |d_j\rangle\}$, where each $|d_j\rangle$ can be either $|01\rangle_j$ or $|10\rangle_j$. The thermal states $|p_T\rangle$ then involve the remaining basis states that contain $|00\rangle_j$ and $|11\rangle_j$ states of dimers.

For the SCL model, the interaction strength γ_{p_S} is proportional to the hopping matrix element $h_{p_S} = \sum_{p_T} \langle p_T | \hat{V} | p_S \rangle$ between the scar $|p_S\rangle$ and the thermal subspace $|p_T\rangle$ [32]. The expression for $\hat{\Gamma}$ can be derived analytically:

$$\hat{\Gamma}_{\text{SCL}} = \sum_{p_S} \sqrt{\gamma_{p_S}} |p_S\rangle \langle p_S| = \sum_{p_S} |p_S\rangle \langle p_S| \sqrt{\sum_{p_T} \langle p_T | \hat{V} | p_S \rangle} = \sum_{p_S} |p_S\rangle \langle p_S| \sqrt{\sum_{j=1}^{N-1} J_{x,j} \hat{P}_{p_S}^{j,j+1}}, \quad (\text{S9})$$

where $\hat{P}_{p_S}^{j,j+1} = \langle d_j | d_{j+1} \rangle$ represents the overlap between two neighboring dimers in $|p_S\rangle$. In the following, we use this expression for $\hat{\Gamma}$ to evaluate the self-energy from the Dyson equation.

A2. Degenerate perturbation theory for the Liouvillean

To explain the structure of Liouvillean QMBS spectra, we set up a degenerate perturbation theory framework. We consider the Liouvillean of the exact QMBS subspace, Eqs. (S5) and (S6), with eigenvalues

$$\lambda_l^{(0)} = i(E_{n_S} - E_{m_S}) = 2ilJ, \quad (\text{S10})$$

where $l = n_S - m_S = -N, -N+1, \dots, N-1, N$. The eigenvalues λ_l are equally spaced along the imaginary axis, with the real part equal to zero.

In the regime $\|\gamma_{\text{eff}} \mathcal{D}' + \mathcal{E}\| \ll \|\mathcal{S}_0\|$, we can use the Liouvillean perturbation theory, in which the traceless Liouvillean eigenvalues for the l th layer are approximately given by $\lambda_l' \approx \lambda_l^{(0)} + \lambda_l^{(1)}$. Here, the zeroth-order eigenvalues are given by the eigenvalues of the unperturbed system in Eq. (S10), while the first-order corrections to the eigenvalues, $\lambda_l^{(1)}$, are obtained by diagonalizing the projection of $\gamma_{\text{eff}} \mathcal{D}' + \mathcal{E}$ to the degenerate subspace of the l th layer, labeled by states $s = 0, 1, 2, \dots, N - |l|$.

First, we consider the dephasing term. Recall that $|\pm\rangle_j = (|0\rangle_j \pm |1\rangle_j) / \sqrt{2}$ and hence we have $\hat{\sigma}_j^z |\pm\rangle_j = |\mp\rangle_j$. The projection of \mathcal{D}' to the l th layer, \mathcal{D}'_l , couples only $|\lambda_{(l,s)}^{(0)}\rangle$ and $|\lambda_{(l,s\pm 1)}^{(0)}\rangle$, hence it can be written as

$$\mathcal{D}'_l = \sum_{s=0}^{N-|l|-1} d_{(l,s)} \left[|\lambda_{(l,s)}^{(0)}\rangle \langle \lambda_{(l,s+1)}^{(0)}| + \text{h.c.} \right], \quad (\text{S11})$$

where $d_{(l,s)}$ represents the coupling coefficient between the s -th and $(s+1)$ -th degenerate eigenstates in the l -momentum layer. Using the translation symmetry of $\sum_i \hat{\sigma}_i^z$, we have

$$d_{(l,s)} = \sum_j^N \left[\langle E_s | \hat{\sigma}_j^z | E_{s+1} \rangle \langle E_{s+|l|} | \hat{\sigma}_j^z | E_{s+|l|+1} \rangle \right] = N \left[\langle E_s | \hat{\sigma}_1^z | E_{s+1} \rangle \langle E_{s+|l|} | \hat{\sigma}_1^z | E_{s+|l|+1} \rangle \right]. \quad (\text{S12})$$

Furthermore, one can show that

$$\langle E_s | \hat{\sigma}_j^z | E_{s+1} \rangle = \frac{\binom{N-1}{s}}{\sqrt{\binom{N}{s} \binom{N}{s+1}}} = \frac{1}{N} \sqrt{(N-s)(s+1)}. \quad (\text{S13})$$

Therefore, we have

$$d_{(l,s)} = \frac{1}{N} \sqrt{(s+1)(N-s)(|l|+s+1)(N-|l|-s)}. \quad (\text{S14})$$

Next, we consider the effect of self-energy. We assume that the thermal subspace is much larger than the scar subspace, and the energy (initially in scar subspace) that leaks into the thermal subspace cannot return. Thus, we have that the off-diagonal term, $\langle E_s | \hat{\Sigma} | E_{s'} \rangle$ with $s \neq s'$, is much smaller than the diagonal term, $\langle E_s | \hat{\Sigma} | E_s \rangle$. $\langle E_s | \hat{\Sigma} | E_s \rangle$ is calculated by Eq. (S7)-(S8). Here, we use approximation as $\langle E_s | \hat{\Sigma} | E_s \rangle \approx \langle E_s | \hat{\Sigma} (E = (-N+2s)J) | E_s \rangle$ and obtained the results by solving the self-consistence equation. The latter diagonal element can be written as

$$\mathcal{E}_l = i \times \text{Diag} \left[\Sigma_{(l,0)}, \Sigma_{(l,1)}, \dots, \Sigma_{(l,N-|l|)} \right], \quad \Sigma_{(l,s)} = \langle E_s | \hat{\Sigma} | E_s \rangle - \langle E_{s+l} | \hat{\Sigma} | E_{s+l} \rangle. \quad (\text{S15})$$

Finally, we obtain the first-order correction to the eigenvalues $\lambda_l^{(1)}$ by diagonalizing the matrix $(\gamma_{\text{eff}} \mathcal{D}'_l + \mathcal{E}_l)$ defined in Eq. (S11) and (S15). As an example, consider the SCL model with $N = 5$ and the layers $l = l''$ with $l'' = -N, -N+2, \dots, N$. For example, layer $l = 3$ holds triple degeneracy, while layer $l = 1$ holds five-fold degeneracy. The corresponding first-order eigenvalues are given by:

- For the exact scar case $\mathcal{E} = 0$, we have $\lambda_{l=3}^{(1)} = 0, \pm \frac{4\sqrt{5}}{5} \gamma_{\text{eff}}$ and $\lambda_{l=1}^{(1)} = 0, \pm \frac{2\sqrt{10}}{5} \gamma_{\text{eff}}, \pm \frac{2\sqrt{46}}{5} \gamma_{\text{eff}}$. The Liouvillian eigenvalues shift along the real axis whenever the dissipative factor γ_{eff} is non-zero;
- For the approximate scar case $\mathcal{E} \neq 0$, the superoperator of the perturbation is more complicated and in the layers $l = l''$ takes the form

$$\begin{aligned} \mathcal{E}_5 + \gamma_{\text{eff}} \mathcal{D}'_5 = (0), \quad \mathcal{E}_3 + \gamma_{\text{eff}} \mathcal{D}'_3 &= \begin{pmatrix} -i\Sigma_{(3,0)} & \sqrt{8/5}\gamma_{\text{eff}} & 0 \\ \sqrt{8/5}\gamma_{\text{eff}} & 0 & \sqrt{8/5}\gamma_{\text{eff}} \\ 0 & \sqrt{8/5}\gamma_{\text{eff}} & i\Sigma_{(3,0)} \end{pmatrix}, \\ \mathcal{E}_1 + \gamma_{\text{eff}} \mathcal{D}'_1 &= \begin{pmatrix} -i\Sigma_{(1,0)} & \sqrt{8/5}\gamma_{\text{eff}} & 0 & 0 & 0 \\ \sqrt{8/5}\gamma_{\text{eff}} & -i\Sigma_{(1,1)} & \sqrt{72/25}\gamma_{\text{eff}} & 0 & 0 \\ 0 & \sqrt{72/25}\gamma_{\text{eff}} & 0 & \sqrt{72/25}\gamma_{\text{eff}} & 0 \\ 0 & 0 & \sqrt{72/25}\gamma_{\text{eff}} & i\Sigma_{(1,1)} & \sqrt{8/5}\gamma_{\text{eff}} \\ 0 & 0 & 0 & \sqrt{8/5}\gamma_{\text{eff}} & i\Sigma_{(1,0)} \end{pmatrix}. \end{aligned} \quad (\text{S16})$$

Analogous expressions for the layers $l = l'$ are:

$$\mathcal{E}_4 + \gamma_{\text{eff}} \mathcal{D}'_4 = \begin{pmatrix} -i\Sigma_{(4,0)} & \gamma_{\text{eff}} \\ \gamma_{\text{eff}} & i\Sigma_{(4,0)} \end{pmatrix}, \quad \mathcal{E}_2 + \gamma_{\text{eff}} \mathcal{D}'_2 = \begin{pmatrix} -i\Sigma_{(2,0)} & \sqrt{9/5}\gamma_{\text{eff}} & 0 & 0 \\ \sqrt{9/5}\gamma_{\text{eff}} & -i\Sigma_{(2,1)} & 8/5\gamma_{\text{eff}} & 0 \\ 0 & 8/5\gamma_{\text{eff}} & i\Sigma_{(2,1)} & \sqrt{9/5}\gamma_{\text{eff}} \\ 0 & 0 & \sqrt{9/5}\gamma_{\text{eff}} & i\Sigma_{(2,0)} \end{pmatrix}. \quad (\text{S17})$$

Then, we have the first-order eigenvalues of the perturbation $(\gamma_{\text{eff}} \mathcal{D}'_l + \mathcal{E}_l)$ as

$$\begin{aligned} \lambda_{l=5}^{(1)} &= 0, \quad \lambda_{l=3}^{(1)} = 0, \pm \sqrt{64\gamma^2/5 - (\Sigma_{(3,0)})^2}, \\ \lambda_{l=1}^{(1)} &= 0, \pm \sqrt{448\gamma^2/25 - \Delta_{1,+}/2 \pm \sqrt{(576\gamma^2/25 + \Delta_{1,-})^2 - 512\Delta_{1,+}\gamma^2/25/2}}, \end{aligned} \quad (\text{S18})$$

and

$$\lambda_{l=4}^{(1)} = \pm \sqrt{4\gamma^2 + (\Sigma_{(4,0)})^2}, \quad \lambda_{l=2}^{(1)} = \pm \sqrt{308\gamma^2/25 + \Delta_{2,+}/2 \pm \sqrt{(64\sqrt{61}\gamma^2/25 + \Delta_{2,-})^2 - 208\Delta_{2,+}\gamma^2/25/2}}, \quad (\text{S19})$$

where $\Delta_{l,\pm} = (\Sigma_{(l,0)})^2 \pm (\Sigma_{(l,1)})^2$ and we used $\gamma_{\text{eff}} = 2\gamma$.

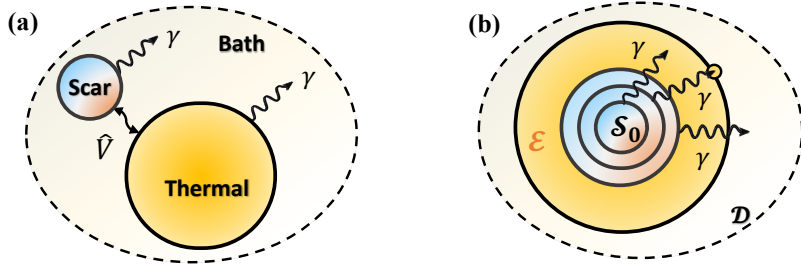


Figure S1. (a) Schematic of a general open quantum many-body system with approximate QMBSs. The scar and thermal subsystems lose their quantum coherence to the bath with the dephasing rate γ , while interacting via the coupling strength V . (b) The Liouville spectral transition originates from the competition between self-energy, \mathcal{E} , and dissipation \mathcal{D} . A set of eigenmodes in Liouville space, denoted by blue concentric circles, are surrounded by the self-energy shell \mathcal{E} , due to the thermal subspace. The latter suppresses those dephasing processes (wavy arrows) that do not exceed the boundary of the self-energy shell (yellow circle).

In $\gamma = 0$ case, the first-order eigenvalues $\lambda_{l=l''}^{(1)}$ are purely imaginary. As the dephasing rate γ increases and exceeds the $\mathbb{P}\mathbb{T}$ -symmetry breaking point, $\lambda_{l=l''}^{(1)}$ will become real value. On the other hand, the first-order eigenvalues $\lambda_{l=l'}^{(1)}$ are already real when $\gamma = 0$, which explains why $\mathbb{P}\mathbb{T}$ -symmetry breaking does not exist in the l' layer.

Furthermore, for $J_{x,j} = 0.1$, the parameters $\Sigma_{(1,0)} \approx 0.0119$, $\Sigma_{(1,1)} \approx 0.0036$, $\Sigma_{(3,0)} \approx 0.0049$ can be calculated by using the non-equilibrium Green's function method in Eq. (S8). The first-order eigenvalue as the dephasing rate increases under these parameters were shown in the main text, illustrating the LPTS breaking point approximately aligns with the numerical results.

Although the $|l| = N$ momentum layer is unrelated to LPTS breaking, for completeness we also derive the perturbative correction for this layer. In this case, we simply use non-degenerate perturbation theory and obtain $\lambda'_N \approx \lambda_N^{(0)} + \lambda_N^{(1)}$, with the first-order eigenvalue given by

$$\begin{aligned}
 \lambda_{|l|=N}^{(1)} &= \pm \left\langle \left\langle \lambda_{(N,0)}^{(0)} \right| (\gamma_{\text{eff}} \mathcal{D}' + \mathcal{E}) \left| \lambda_{(N,0)}^{(0)} \right\rangle \right\rangle = \pm \gamma_{\text{eff}} \sum_j^N (\langle E_N | \hat{\sigma}_j^z | E_N \rangle \times \langle E_0 | \hat{\sigma}_j^z | E_0 \rangle) \pm i \left(\langle E_N | \hat{\Sigma} | E_N \rangle - \langle E_0 | \hat{\Sigma} | E_0 \rangle \right) \\
 &= \pm \gamma_{\text{eff}} \sum_j^N \langle + |^{\otimes N} \hat{\sigma}_j^z | + \rangle^{\otimes N} \langle - |^{\otimes N} \hat{\sigma}_j^z | - \rangle^{\otimes N} \pm i \left(\langle E_N | \hat{\Sigma} | E_N \rangle - \langle E_0 | \hat{\Sigma} | E_0 \rangle \right) \\
 &= \pm i \left(\langle E_N | \hat{\Sigma} | E_N \rangle - \langle E_0 | \hat{\Sigma} | E_0 \rangle \right).
 \end{aligned} \tag{S20}$$

These expressions show that the first-order eigenvalues are purely imaginary. This implies that eigenvalues in the momentum layer of $|l| = N$ move along the imaginary axis under the perturbation $(\gamma_{\text{eff}} \mathcal{D}' + \mathcal{E})$.

A3. Scaling behavior

From the perspective of perturbation theory, the LPTS breaking phenomenon originates from the competition between dissipation $\gamma_{\text{eff}} \mathcal{D}'$ and the self-energy \mathcal{E} , as summarized in Fig. S1. We can estimate the typical LPTS breaking point:

$$\bar{\gamma}_*^S \|\mathcal{D}'\| \sim \|\mathcal{E}\|, \tag{S21}$$

where $\|\hat{A}\| = \sqrt{\lambda_{\max}(\hat{A}^\dagger \hat{A})}$ refers to the matrix norm of \hat{A} . The dissipation superoperator scales with N , $\|\mathcal{D}'\| = \sum_{j=1}^N \|\hat{\sigma}_j^z \otimes \hat{\sigma}_j^z\| \sim N$. To estimate the scaling of self-energy for large N , recall the self-consistency condition, Eq. (S8), and focus on the SCL model, with \hat{S}_0 in Eq. (S4). The maximal energy is NJ , so we have $\|E\hat{I} - \hat{S}_0\|$ scaling as N . According to Eq. (S9),

$$\|\hat{\Gamma}\| = \sqrt{\max \left(\sum_{j=1}^{N-1} J_{x,j} \hat{P}_{ps}^{j,j+1} \right)}. \tag{S22}$$

The possible value of $\hat{P}_{ps}^{j,j+1}$ is 0 and 1, so $\|\hat{\Gamma}\| = \sqrt{\sum_{j=1}^{N-1} J_{x,j}} \sim \sqrt{N}$, where we assume that all the couplings $J_{x,j}$ are at the same order of magnitude. Approximately, from the self-consistence equation, we assume that $\|\hat{\Sigma}\|$ increase slower than $\|E\hat{I} - \hat{S}_0\|$, and we have

$$\|\hat{\Sigma}\| \times \|E\hat{I} - \hat{S}_0\| \sim \|\hat{\Gamma}\|^2. \quad (\text{S23})$$

Then we obtain that $\|\hat{\Sigma}\| \sim \text{const.}$, which agrees with the assumption we made that $\|\hat{\Sigma}\|$ increase slower than $\|E\hat{I} - \hat{S}_0\|$. Finally, we use Eq. (S3) and have $\|\mathcal{E}\| \sim \text{const.}$ in large- N limit, so that $\bar{\gamma}_*^S \sim N^{-1} \sim L^{-1}$. As discussed in the main text, this scaling is in stark contrast with $\bar{\gamma}_* \sim D^{-2}$ for thermal eigenvalues, where D is the Hilbert space dimension.

A4. PXP model

The scar subspace of the PXP model can also be approximately described using the Hamiltonian decomposition in Eq. (S1) and the Liouvillean in Eq. (S4). Within this approximation, we can directly apply our analysis above by simply replacing the expression for the self-energy:

$$\hat{\Gamma}_{\text{PXP}} = \sum_{ps} |ps\rangle \langle ps| \sqrt{\prod_{j=1}^{N-1} \langle ps | \hat{P}_j \hat{P}_{j+1} | ps \rangle} = \sqrt{J \prod_{j=1}^{N-1} \hat{P}_j \hat{P}_{j+1}}, \quad (\text{S24})$$

where $\hat{P}_j = (1 - \hat{\sigma}_j^z)/2$. This approximation successfully explains some features of the PXP Liouvillean spectra, e.g., the asymmetry about the imaginary axis, which can be traced back to the following property of the self-energy:

$$\langle E_{ns} | \hat{\Sigma}_{\text{PXP}} | E_{ns} \rangle \neq \langle E_{N-ns} | \hat{\Sigma}_{\text{PXP}} | E_{N-ns} \rangle. \quad (\text{S25})$$

By contrast, the analogous Eq. (S25) in the SCL model is obeyed as an equality, consistent with the symmetry of the SCL Liouvillean spectrum.

However, the above approximation is not expected to be quantitatively accurate as it ignores the effect of the Rydberg constraint on the PXP Hilbert space. The constraint makes it challenging to analytically perform the perturbation theory for the PXP Liouvillean. Furthermore, to obtain quantitatively accurate results, the QMBS Hamiltonian \hat{S}_0 should be replaced by an effective spin-1 paramagnet in the dimerized picture [24].

B. Symmetries of Liouvillean eigenmodes

In this section, we study the symmetry properties of the Liouvillean eigenstates. Recall that the unperturbed \mathcal{S}_0 has eigenstates $|\lambda_{(l,s)}^{(0)}\rangle\rangle = |E_s\rangle \otimes |E_{l+s}\rangle$. Take $N = 3$ case as an example. There are $N + 1 = 4$ eigenstates of $\hat{\mathcal{S}}_0$ in the maximal spin representation:

$$\begin{aligned} |E_0\rangle &= |---\rangle, & |E_1\rangle &= \frac{1}{\sqrt{3}}(|+--\rangle + |-+-\rangle + |--+\rangle), \\ |E_2\rangle &= \frac{1}{\sqrt{3}}(|++-\rangle + |+-+\rangle + |--++\rangle), & |E_3\rangle &= |+++ \rangle, \end{aligned} \quad (\text{S26})$$

with energies $-3J, -J, J$ and $3J$, respectively. The Liouvillean spectrum of (\mathcal{S}_0) has a seven-layer structure with (imaginary) eigenvalues $0, \pm 2J, \pm 4J, \pm 6J$.

The Liouvillean spectrum of $(\mathcal{S}_0 + \gamma\mathcal{D}')$ maintains the seven-layer structure, but now includes eigenvalues with non-zero real parts. In the layer of $l = 1$, there are two types of Liouvillean eigenmodes. Both of them are the linear superpositions of $|E_0\rangle \otimes |E_1\rangle$, $|E_1\rangle \otimes |E_2\rangle$, and $|E_2\rangle \otimes |E_3\rangle$, but with different coefficients. One of them is purely imaginary,

$$\frac{1}{\sqrt{2}}|E_0\rangle \otimes |E_1\rangle - \frac{1}{\sqrt{2}}|E_2\rangle \otimes |E_3\rangle, \quad (\text{S27})$$

while the other one is more complex:

$$\frac{1}{2}|E_0\rangle \otimes |E_1\rangle + \frac{1}{2}|E_2\rangle \otimes |E_3\rangle \pm \frac{1}{\sqrt{2}}|E_1\rangle \otimes |E_2\rangle. \quad (\text{S28})$$

Note that the former one does not include components of $|E_1\rangle \otimes |E_2\rangle = |\lambda_{(1,1)}^{(0)}\rangle\rangle$. More generally, we find that the pure imaginary Liouvillean eigenmodes in layer l have zero overlap with those $|\lambda_{(l,s)}^{(0)}\rangle\rangle$ where s is odd.

Furthermore, we find that the LPTS breaking phenomenon exists only in layers where $(N - |l|)$ is even, i.e., where $l = l''$. Thus, studying the Liouvillean eigenmodes $\{|\lambda_{(l,s)}^{(0)}\rangle\rangle\}$ in layer l'' can help us to understand the nature of LPTS breaking. We define a special Liouvillean vector

$$|\zeta\rangle\rangle = \sum_{l''} \frac{1}{\sqrt{N-1}} |\lambda_{(l'',1)}^{(0)}\rangle\rangle, \quad (\text{S29})$$

where the $N - 1$ normalizing factor counts the total number of layers with LPTS breaking. We confirmed, for the SCL model and $\gamma < \gamma_*^S$, the overlap between $|\zeta\rangle\rangle$ and the eigenmodes in the layer l'' is nearly zero. Once $\gamma > \gamma_*^S$, the overlap rises sharply to a finite number. This behavior mimics that of the real part of Liouvillean eigenvalues.

According to the general symmetry classification of Lindbladians [88], the operator responsible for \mathbb{PT} symmetry is the \mathcal{T}_- superoperator that obeys:

$$\mathcal{T}_- \mathcal{L} \mathcal{T}_-^{-1} = -\mathcal{L}, \quad \mathcal{T}_-^2 = \pm 1. \quad (\text{S30})$$

The explicit form of \mathcal{T}_- for the SCL model is

$$\mathcal{T}_- = \sqrt{p_x} \left[\left(\prod_i \hat{\sigma}_i^x \right) \otimes \hat{I} \right] \mathcal{K}, \quad (\text{S31})$$

where \mathcal{K} is the Liouvillean complex-conjugation operator, $\mathcal{K} \mathcal{L} \mathcal{K}^{-1} = \mathcal{L}^*$, and \hat{I} is the identity matrix. The factor $p_x = \pm 1$, which makes $\mathcal{T}_-^2 = \pm 1$, respectively.

When $\gamma = 0$, all eigenmodes are symmetric: $\lambda' = -(\lambda')^*$ and $\mathbb{PT}|\lambda'\rangle\rangle = |-(\lambda')^*\rangle\rangle$. Thus, $|-(\lambda')^*\rangle\rangle$ is degenerate with $|\lambda'\rangle\rangle$ and these lie on the imaginary axis. As the dephasing rate γ increases until it exceeds the critical point γ_*^S , the symmetry of $\lambda' = -(\lambda')^*$ is broken, while the eigenvectors continue to be related via $\mathbb{PT}|\lambda'\rangle\rangle = |-(\lambda')^*\rangle\rangle$ remains. This indicates that, after the critical point, a few pairs of degenerate eigenvalues move symmetrically away from the imaginary axis along the real axis. In addition, a few eigenvalues stay at the imaginary axis regardless of the magnitude of γ . For each momentum subspace, these eigenmodes can be found using the condition of

$$\mathbb{PT}|\lambda'\rangle\rangle = |\lambda'\rangle\rangle, \quad \lambda' = -(\lambda')^*. \quad (\text{S32})$$

We note that, for the PXP model, we cannot find a \mathcal{T}_- operator that satisfies Eq. (S30). Without \mathcal{T}_- symmetry, the Liouvillean spectrum is intrinsically asymmetric about the imaginary axis [88], as confirmed by the numerical simulations.

C. The origin of LPTS breaking

While a broader understanding of general types of dissipation and their effects on QMBs is beyond the scope of current work, one immediate question is whether our results in the main text can be explained more simply by imposing certain approximations, such as considering the effective non-Hermitian description (as opposed to the full Lindblad dynamics).

In Fig. S2 we numerically argue that LPTS breaking due to dephasing does not exist in the non-Hermitian approximation which adds the term $i\gamma \sum_{j=1}^L \hat{\sigma}_j^z$ to the Hamiltonian. From the form of this term, it is clear that for the SCL model in the sector with conserved magnetization $\sum_{j=1}^L \hat{\sigma}_j^z = 0$, the non-Hermitian operator in the spin z -direction has no effect on the Liouville spectrum. This is confirmed in Fig. S2, which also shows that the non-Hermitian PXP model immediately breaks LPTS by a very small $\gamma = 10^{-4}$, in stark contrast with the results for its Liouvillean spectrum in the main text.

D. Exact vs. approximate scars in SCL and PXP models

For the SCL model, in the main text we emphasized a significant difference in the Liouvillean spectra of the two subspaces with reflection symmetry $p = \pm 1$, and also between the cases of approximate ($J_{x,j} \neq 0$) vs. exact ($J_{x,j} = 0$)

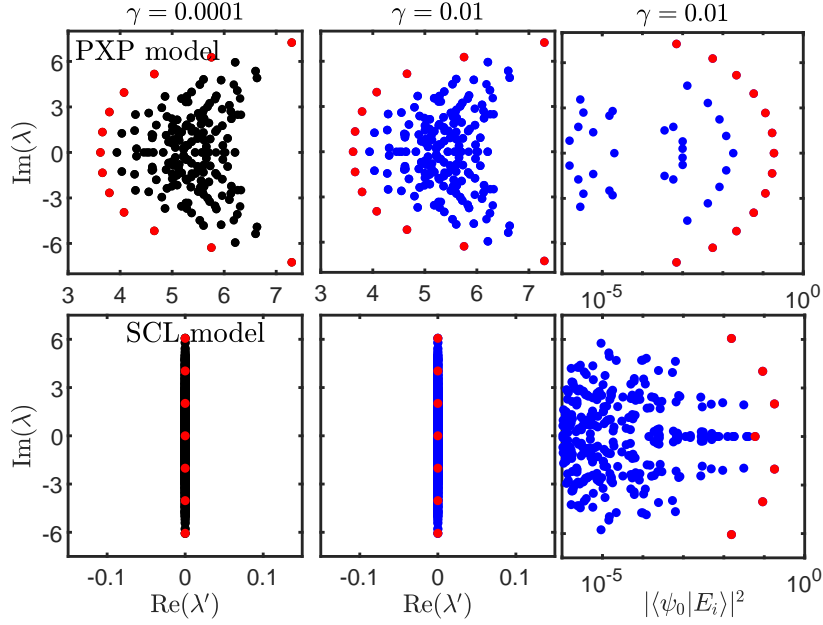


Figure S2. The Liouvillian spectra of the effective non-Hermitian Hamiltonians for the PXP model and SCL model ($J_{x,j} = 0.1$) at two dephasing rates $\gamma = 0.0001, 0.01$. The black and blue dots indicate the spectra of thermal states, while the red dots denote the approximate QMBSs. The system size is $L = 12$. Other parameters are the same as the main text

QMBSs. We highlight these differences in more detail in Fig. S3. In the odd subspace $p = -1$, most approximate scars exhibit LPTS under weak dissipation, while in the even subspace $p = +1$ they have immediately broken LPTS. Under strong dissipation, the behavior of the two sectors tends to be consistent. In addition, we also observe that the maximum overlaps of scars are uniformly distributed in the Liouvillian spectral range across different subspaces. In the case of weak dissipation, more scars in $p = -1$ odd subspace approach the zero point, $\text{Re}(\lambda'/\gamma) = 0$. However, as the dephasing rate increases, they gradually move away from zero.

For the PXP model, also shown in Fig. S3, we find qualitatively similar behavior to the SCL model, with a few minor differences. First, the LPTS breaking occurs in different momentum q sectors under translation, rather than inversion symmetry p in the SCL model. Second, there is no way to directly tune between approximate and exact QMBS limits. Instead, as a proxy for the latter, we consider a deformed PXP model (DPXP), introduced in the main text. With these provisos, the behavior of the PXP model largely mirrors that of SCL model, with the main difference that $\mathbb{P}\mathbb{T}$ symmetry is only approximately obeyed, e.g., see the scar states with momentum $q = 0$ in Fig. S3(a). As we explained above, this is attributed to a lack of \mathcal{T}_- symmetry of the PXP Liouvillian. Nevertheless, these scarred eigenvalues still exhibit clustering around the imaginary axis at weak dephasing rates, giving rise to a certain level of robustness of QMBS signatures in dissipative dynamics, just like for the SCL model with $J_{x,j} \neq 0$.

E. Further numerical results on Liouvillian spectra of different models

Spontaneous LPTS breaking can also be observed in the approximate scar states of a 1D tilted Fermi-Hubbard (TFH) model, Fig. S4, whose Hamiltonian (after the Jordan-Wigner transformation) is [35]

$$\hat{H}_{\text{TFH}} = J \sum_j^L \left[\hat{\sigma}_{j,\uparrow}^+ \hat{\sigma}_{j,\uparrow}^- \hat{P}_{j,\downarrow} (1 - \hat{P}_{j,\downarrow}) - \hat{\sigma}_{j,\downarrow}^+ \hat{\sigma}_{j,\downarrow}^- \hat{P}_{j,\uparrow} (1 - \hat{P}_{j,\uparrow}) \right], \quad (\text{S33})$$

where the action of $\hat{\sigma}_{j,\uparrow(\downarrow)}^+$ is to create an excitation on site j with Jordan-Wigner spin up or down. $\hat{P}_{j,\uparrow(\downarrow)} = (\hat{I} + \hat{\sigma}_{j,\uparrow(\downarrow)}^z)/2$ the projector on the excited state of the Jordan-Wigner spin.

Beyond QMBSs, our conclusions are also applicable to Hilbert space fragmentation (HSF). As an example of HSF,

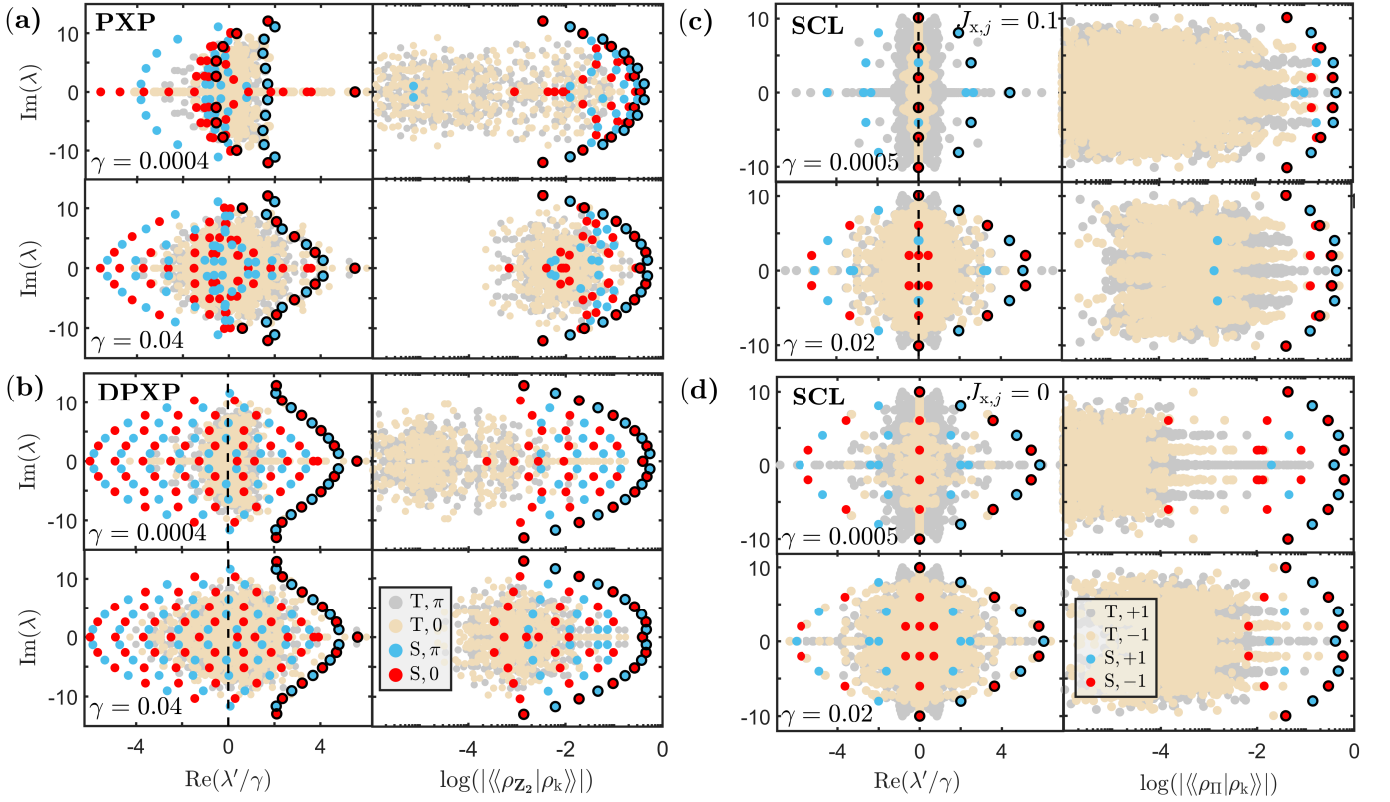


Figure S3. (a)-(b) The Liouvillean spectra (left panel) and the overlap with $|\mathbb{Z}_2\rangle \otimes |\mathbb{Z}_2\rangle$ (right panel) corresponding to two dephasing rates, $\gamma = 0.0004, 0.04$, of the PXP model and DPXP model. The scar (S) and thermal (T) states are labeled according to $q = 0, \pi$ momenta under translation, as indicated in the legend. (c)-(d) The case of the SCL model with $J_{x,j} = 0, 0.1$. The states are labeled by $p = \pm 1$, indicating the inversion symmetry is even (odd). The overlap is with the state $|\Pi\rangle \otimes |\Pi\rangle$, defined in the main text. In all plots, the black boundary dots indicate scar states with the local maximum overlap with the chosen initial state. The system size is $L = 10$ in all plots.

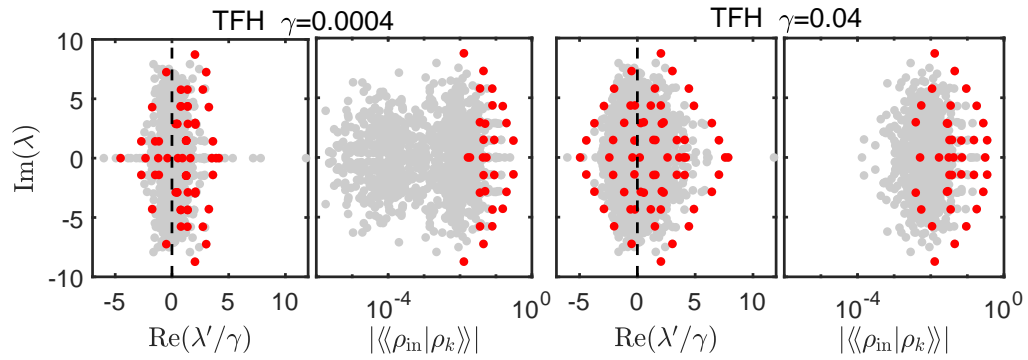


Figure S4. 1D tilted Fermi-Hubbard (TFH) model, Eq. (S33), for two different dephasing rates. The gray dots indicate the Liouvillean spectra of thermal states, while the red dots indicate the spectra of scar states. The system size is $L = 6$.

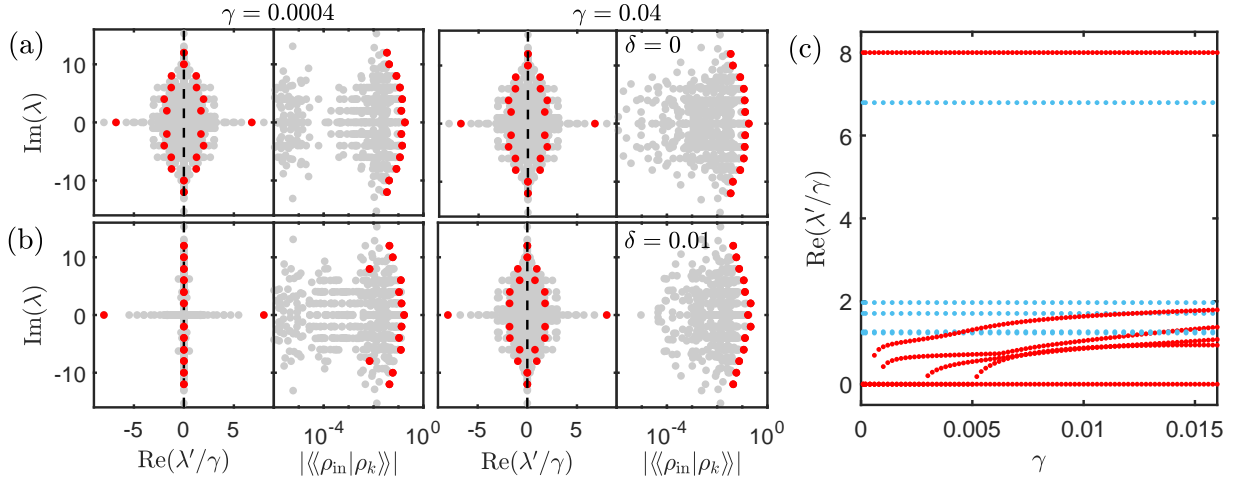


Figure S5. Hilbert space fragmentation in the frustrated Heisenberg ladder model (S34). (a) and (b) correspond to the case of $\eta = 0$ and $\eta = 0.01$, respectively. The gray dots indicate the Liouville spectra of all states, while the red dots denote the spectra of a few typical local HSF states. (c) The variation of the Liouvillean spectrum $\text{Re}(\lambda'/\gamma)$ of a few typical local HSF states with the dephasing rate γ . The red (blue) dots are $\eta = 0.01$ (0). The system size is $L = 8$ and the parameter $J = 1$.

we consider the spin-1/2 frustrated Heisenberg ladder [91]:

$$\begin{aligned}
 \hat{H}_{\text{FLH}} &= \hat{H}_+ + \hat{H}_- + \hat{H}_v + \hat{H}_x, \\
 \hat{H}_\pm &= J(1 - \eta) \sum_{j=1}^N [(\hat{\sigma}_{j,\pm}^+ \hat{\sigma}_{j+1,\pm}^- + \text{h.c.}) + \hat{\sigma}_{j,\pm}^z \hat{\sigma}_{j+1,\pm}^z], \\
 \hat{H}_v &= \frac{1}{2} J \sum_{j=1}^N [(\hat{\sigma}_{j,-}^+ \hat{\sigma}_{j,+}^- + \text{h.c.}) + \hat{\sigma}_{j,-}^z \hat{\sigma}_{j,+}^z], \\
 \hat{H}_x &= J(1 + \eta) \sum_{j=1}^N [(\hat{\sigma}_{j,\pm}^+ \hat{\sigma}_{j+1,\mp}^- + \text{h.c.}) + \hat{\sigma}_{j,\pm}^z \hat{\sigma}_{j+1,\mp}^z].
 \end{aligned} \tag{S34}$$

When η equals zero, we have the complete frustration structure, resulting in a disconnected Hilbert space fragments. Small but non-zero η corresponds to a weakly-connected HSF.

In Fig. S5, we see that when the local HSF is not coupled with the thermalization part, the dephasing system remains in a state of LPTS breaking, while conversely, a clear process of LPTS breaking occurs. It should be noted that the red dots in Fig. S5(a)-(b) represent a few typical local HSF states and do not include all local HSF states.

F. Detail of the imbalance dynamics

The LPTS breaking can also be manifested through the dynamical behavior of the density imbalance, $I(t) = (1/L) \sum_j \langle \rho(0) | \hat{\sigma}_j^z \otimes \hat{\sigma}_j^z | \rho(0) \rangle \langle \rho(t) | \hat{\sigma}_j^z \otimes \hat{\sigma}_j^z | \rho(t) \rangle$, for some initial state $|\rho(0)\rangle$. The imbalance dynamics in dissipation-free scenarios exhibit the form of a damped oscillation for special (scarred) initial states, i.e., $|\Pi\rangle \otimes |\Pi\rangle$ state in the SCL model and $|\mathbb{Z}_2\rangle \otimes |\mathbb{Z}_2\rangle$ state in the PXP model. These QMBS oscillations can be fitted by using $\tilde{I}(t) = \exp(-\beta t) \cos(\omega t)$ over one time periods in Figs. S6(a)-(b).

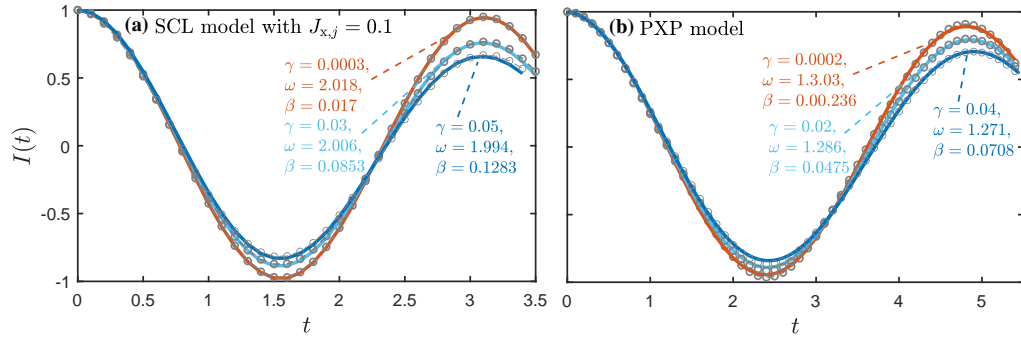


Figure S6. (a)-(b): The time evolution of density imbalance $I(t)$ for SCL and PXP models for different pure dephasing rates γ . The gray dashed-dot represents the fitting function $\bar{I}(t)$. The coefficients (β, ω) of the imbalance fitting function $\bar{I}(t)$ are shown in panel. The system size is $L = 14$.